Microwave-Assisted Synthesis of Few-Layer Black Phosphorus and Its Application in Solar Cells

by

Munkhjargal Bat-Erdene

Thesis
Submitted to Flinders University
for the degree of

Master of Science

College of Science and Engineering

December, 2017

Dedication

This thesis is dedicated to my parents and also to my husband (Munkhbayar Batmunkh) and son (Khuslen Munkhbayar).

Table of Contents

Declaration

I certify that this Thesis contains no material which has been accepted for the award of any other degree or diploma in any university or other tertiary institution and, to the best of my knowledge and belief, contains no material previously published or written by another person, except where due reference has been made in the text. In addition, I certify that no part of this work will, in the future, be used in a submission for any other degree or diploma in any university or other tertiary institution without the prior approval of Flinders University.

Munkhjargal Bat-Erdene

Acknowledgements

It would not have been possible for me to write this Thesis without the great support of many people around me, to only some of whom it is possible to give particular mention here.

First of all, I would like to express my greatest gratitude to Professor Joe Shapter for being a wonderful supervisor/mentor and for enabling me to reach this milestone. I therefore attribute my success in this Master's study to his excellent scientific guidance and continuous encouragement. He is also a wonderful role model both professionally and personally.

I would also like to thank Dr. Munkhbayar Batmunkh, who has supported me throughout this journey of Master's study. Not only his valuable guidance and excellent support in my research, but also his never-ending encouragement was the key motivation to successfully complete this journey.

Further, I would like to express my gratitude to our lab members and colleagues, who have made my Master's study fruitful at Flinders University. In particular, I would like to thank Dr. Cameron Shearer, Dr. Chris Gibson, Dr. Mahnaz Dadkhah and Leping Yu for their great assistance, invaluable advice and constructive comments for all of my work that has been carried out during my study. I would also like to extend my thank to my colleagues Hui-Yin Lim, Tom Grace, Dr. Zahrah Alhalili, Dr. Ashley Slattery, Alex Sibley and others for being wonderful friends and helping me succeed.

The excellent research environment and world-class research facilities at Flinders University have enabled me to collaborate with leading researchers in the field including Dr. Sherif Tawfik, Dr. Marco Fronzi, Prof. Mike Ford (@UTS) and others.

I also acknowledge the financial support and tuition waiver I have received during my study at Flinders University. I must also acknowledge the use of South Australian nodes of the Australian Microscopy & Microanalysis Research Facility (AMMRF) and the Australian National Fabrication Facility (ANFF) at Flinders University.

Last but not least, none of this would have been possible without the support of my parents and my parents-in-law. Words cannot express the feelings I have for them for their unconditional love and endless support. I am very lucky because I have Munkhbayar Batmunkh as my loving husband and Khuslen Munkhbayar as my lovely son in my life.

Summary

Breakthroughs in materials science will undoubtedly have a significant impact on the future development of technology since the research into nanostructured materials is currently playing a central role in the revolutionary technologies. Since the discovery of graphene, two-dimensional (2D) materials have emerged as important advanced materials due to their unique structures and fascinating properties. Phosphorene – few-layer black phosphorus (BP) – has been introduced as a new member to the family of elemental 2D layered materials. Phosphorene is attracting tremendous interest from the scientific community and has shown great promise in a diverse range of applications owing to its unique structure and excellent properties. One of the most promising applications for phosphorene and phosphorene based materials is photovoltaic (PV). However, the limited number of established experimental procedures to prepare phosphorene restricts its successful application in solar cells. Therefore simple production of high quality, stable and scalable 2D phosphorene sheets is extremely challenging.

In this project, we demonstrated a facile, novel and efficient way to prepare solution processable phosphorene flakes in N-methyl-2-pyrrolidone (NMP) solvent using a microwave (MW)-assisted method in ambient conditions. The as-prepared phosphorene flakes were highly crystalline, atomically thin and exhibit low oxidation level in ambient condition. More importantly, this MW-assisted liquid-phase exfoliation method requires a very short processing time (~10 min) and does not involve the use of any surfactant or ultrasonication to obtain stable phosphorene dispersion.

As a proof of concept, our MW-exfoliated phosphorene sheets were introduced into single-walled carbon nanotube-silicon (SWCNT-Si) heterojunction solar cells (HJSCs) for the first time. The NMP based phosphorene sheets remain stable after mixing with water based SWCNT dispersion for device fabrication. Because of their unique structure and *p*-type dominated conduction, the phosphorene sheets incorporated SWCNT-Si solar cells exhibited remarkably high power conversion efficiency (PCE) of 9.37%, whereas the control device fabricated without

phosphorene showed a PCE of 7.52%. We carried out a wide range of experimental analysis, combined with theoretical density-functional theory (DFT) calculation, to provide a molecular level understanding of the influence of phosphorene sheets in SWCNT-Si solar cells. Overall, this Master's project is extremely important in that it has the potential to facilitate future development of phosphorene research.

List of publications

Peer-reviewed international journal publications I have authored and co-authored during my Master's study at Flinders University.

1] **Munkhjargal Bat-Erdene**, Munkhbayar Batmunkh, Cameron J. Shearer, Sherif Abbas, Michael J. Ford, LePing Yu, Alex J. Sibley, Ashley D. Slattery, Jamie S. Quinton, Christopher G. Gibson, and Joseph G. Shapter, Efficient and fast synthesis of few-layer black phosphorus flakes via microwave-assisted liquid-phase exfoliation, *Small Methods*, **2017**, *1*, 1700260.

2] **Munkhjargal Bat-Erdene**, Munkhbayar Batmunkh, Sherif A. Tawfik, Marco Fronzi, Michael J. Ford, Cameron J. Shearer, LePing Yu, Mahnaz Dadkhah, Jason R. Gascooke, Christopher G. Gibson and Joseph G. Shapter, Efficiency enhancement of single-walled carbon nanotube-silicon heterojunction solar cells using microwave-exfoliated few-layer black phosphorus, *Advanced Functional Materials*, **2017**, DOI: 10.1002/adfm.201704488.

3] Munkhbayar Batmunkh, **Munkhjargal Bat-Erdene** and Joseph G. Shapter, Black phosphorus: synthesis and application for solar cells, *Advanced Energy Materials*, **2017**, DOI: 10.1002/aenm.201701832.

4] Munkhbayar Batmunkh, Thomas J. Macdonald, Cameron J. Shearer, **Munkhjargal Bat-Erdene**, Yun Wang, Mark J. Biggs, Ivan P. Parkin, Thomas Nann, and Joseph G. Shapter, Carbon nanotubes in TiO_2 nanofiber photoelectrodes for high performance perovskite solar cells, *Advanced Science*, **2017**, *4*, 1600504.

5] Munkhbayar Batmunkh, Cameron J. Shearer, **Munkhjargal Bat-Erdene**, Mark J. Biggs and Joseph G. Shapter, Single-walled carbon nanotubes enhance the efficiency and stability of nanocrystalline TiO_2 photoelectrode based perovskite solar cells, *ACS Applied Materials & Interfaces*, **2017**, *9*, 19945–19954.

6] Munkhbayar Batmunkh, **Munkhjargal Bat-Erdene** and Joseph G. Shapter, Phosphorene and phosphorene based materials – prospects for future application, *Advanced Materials*, **2016**, *28*, 8586–8617. *ChemInform Abstract*.

7] Munkhbayar Batmunkh, Aabhash Shresta, **Munkhjargal Bat-Erdene**, Md. J. Nine, Cameron J. Shearer, Christopher T. Gibson, Ashley D. Slattery, Sherif A. Tawfik, Michael J. Ford, Shizhang Qiao, Sheng Dai, and Joseph G. Shapter, Electrocatalytic activity of ultrathin 2D phosphorene based heteroelectrocatalyst for photoelectrochemical cells, **2018**, Submitted Manuscript.

Parts of the above publications have been reproduced in this Thesis as follows:

- Chapter 1 contains parts of [3] and [6].
- Chapter 2 contains parts of [1] and [2].
- Chapter 3 contains parts of [1] and [2].
- Chapter 4 contains parts of [3] and [6].

Chapter 1.

Introduction

1.1. Overview

Materials science has played, and is still playing, a major role in the development of revolutionary technologies. New and advanced materials will undoubtadly have significant impact on the future development of many technologies. In 2004, a notable discovery was made by Novoselov and Geim who successfully extracted a single layer of carbon atoms arranged in a hexagonal lattice from bulk graphite.[1] This work resulted in the *Nobel Prize in Physics* in 2010. Graphene, a monolayer of carbon atoms arranged in a hexagonal lattice, is the thinnest material in the universe and has many fascinating properties.[2] Since then, two-dimensional (2D) layered materials have been widely explored and now emerged as important advanced materials due to their unique structures and extraordinary properties.[3-5]

The successful demonstration of few-layer black phosphorus (FL-BP), called "phosphorene", has attracted a great deal of research interest owing to its natural semiconducting properties.[6, 7] BP is an ambipolar semiconductor with a predicted tunable direct band gap of 0.3 eV for the bulk and 2 eV for a monolayer depending on the interlayer stacking pattern.[8, 9] Also, BP shows strong in-plane anisotropy unlike other 2D materials and balances outstanding properties such as excellent carrier mobility, high ON/OFF ratio and thermoelectric performance.[8-11] However, research into the fundamental properties and potential applications of phosphorene are still at an early stage.

In this Thesis, we have investigated liquid-phase exfoliation of bulk BP to prepare solution processed few-layer phosphorene sheets using a microwave (MW)-assited system and explored their feasibility in photovoltaic devices.

1.1.1. Structure

Phosphorene is composed of individual layers held together by van der Waals forces in lieu of covalent or ionic bonds (see Figure 1-1a). In phosphorene, phosphorus forms sp^3 bonding with a lone pair of valence electrons in each phosphorus atom. Phosphorene has a puckered structure along the armchair direction (z-axis, (Figure 1-1b)), but it appears as a bilayer configuration along the zigzag direction (x-axis, (Figure 1-1b)). The lattice constants along the two perpendicular directions are

different, at a = 4.52 ± 0.05 Å and b = 3.31 ± 0.03 Å ("a" and "b" are shown in Figure 1-1b), respectively, depending on the number of layers.[7, 9] Therefore, it is clear that the geometric properties of phosphorene can be tuned as a function of layer number. For monolayer phosphorene, the connecting bond length (*R1*) value is 2.244 Å which is very close to that of the adjacent *P*–*P* bond length (*R2*) (2.224 Å).[8, 12]

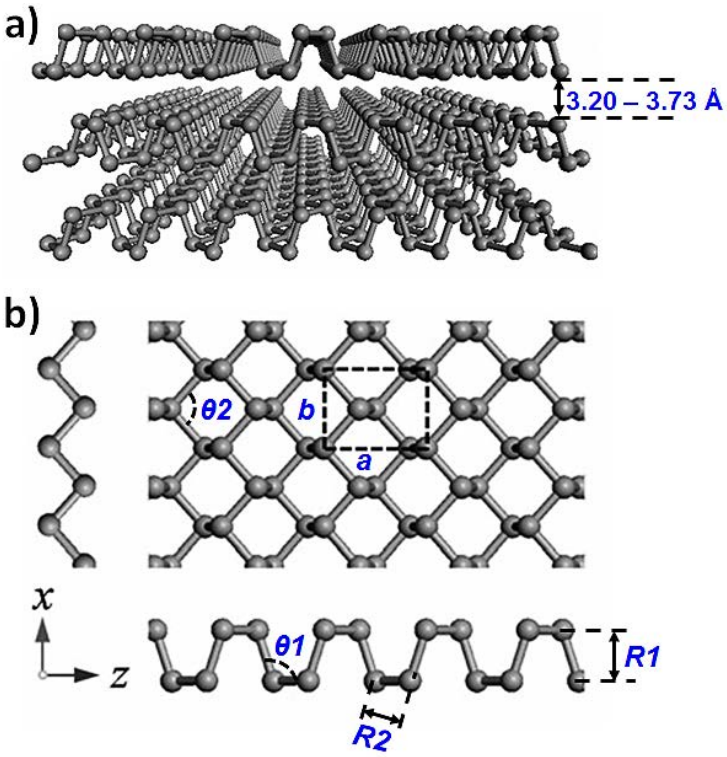

Figure 1-1. (a) The puckered structure of three-layer phosphorene and (b) top view of monolayer phosphorene.[12] The x and z axis are along the zigzag and armchair directions, respectively.

1.1.2. Properties

Phosphorene has been considered more favourable than other 2D materials in a wide range of applications based on its many excellent properties. To demonstrate that phosphorene holds great potential for many applications, Table 1-1 compares the electronic and mechanical properties of several 2D materials including phosphorene, graphene, MoS_2, WSe_2 and *h*-BN.

Table 1-1. Summary of fundamental properties of different 2D materials. The values listed in this Table were reported with the corresponding references in our review article.[8]

	Phosphorene	Graphene	MoS_2	WSe_2	*h*-BN
Type	Semiconductor	Semimetal	Semiconductor	Semiconductor	Insulator
Bandgap (eV)*	0.3 – 2.0	0	1.2 – 1.8	1.2 – 1.7	5.9
Carrier mobility, ($cm^2 \cdot V^{-1} \cdot s^{-1}$)	~1000	~2 x 10^5	10 – 200	140 – 500	–
ON/OFF ratio	10^3 – 10^5	5.5 – 44	10^6 – 10^8	10^4 – 10^6	–
Thermal conductance ($W \cdot m^{-1} \cdot K^{-1}$)	10 – 36	~5 x 10^3	34.5 – 52	9.7	250 – 360
Thermoelectric performance, ZT	1 – 2.5	~0	0.4	0.91	–
Young's Modulus (GPa)	35 – 166	1000	270 ± 100	75 – 195	220 – 880
Fracture strain (%)	24 – 32	27 – 38	25 – 33	26 – 37	24
Conduction type	Ambipolar	Ambipolar	n–type	Ambipolar	–

As depicted in Table 1-1, although phosphorene does not exhibit the ideal values for all parameters for a variety of applications, it does balance excellent properties over these parameter spaces for various applications such as solar cells, batteries, transistors and so on. For example, graphene shows the highest carrier mobility, thermal conductivity and stiffness, but its ON/OFF ratio is very low due to by its zero-bandgap. On the other hand, MoS_2 and WSe_2 show very high ON/OFF ratio due to their high bandgap. However, the low conductivities of these materials limit their widespread applications in many fields. Insulating properties of *h*-BN hinder its potential applications, especially in solar cells. Indeed, 2D phosphorene possesses a comprehensive range of excellent chemical, physical, optical and mechanical properties, which can be useful for optoelectronic device applications. High charge mobility is one of the key prerequisites for the materials for use in solar cell.

Therefore due to its high charge mobility, phosphorene could be an excellent candidate for solar cell applications. The carrier mobility of phosphorene at room temperature is ~300 $cm^2 \cdot V^{-1} \cdot s^{-1}$ and can be increased to ~1000 $cm^2 \cdot V^{-1} \cdot s^{-1}$ at 120 K.[6, 7, 9, 13]

The optical absorption of phosphorene depends on the orientation. According to He et al.,[14] the absorption coefficient in the zigzag direction is approximately 10 times lower than the armchair direction. Moreover, the diffusion coefficient of the photo-carrier along the armchair direction is nearly 16 times higher than that in the zigzag direction. The review article published by Rahman et al.[15] predicted that such unique optical properties of phosphorene will be useful for photo-energy-conversions such as photocatalysis and PV applications. Another unique feature of phosphorene is its highly anisotropic band dispersion in the Brillouin zone (BZ) near the Fermi level.[16]

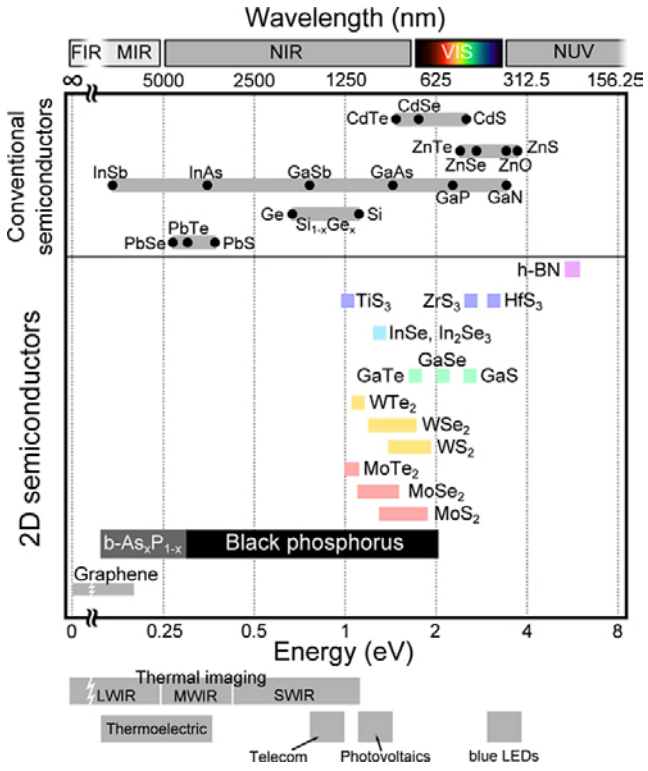

Figure 1-2. The bandgap values of different semiconductors and some 2D layered materials. At the bottom, the range of bandgap values required for certain applications are highlighted.[19]

The energy bandgap is the key parameter of the materials for many device applications including solar cells. The bandgap of phosphorene is highly tunable from 0.3 eV to 2.0 eV depending on the interlayer stacking pattern. This bandgap value of phosphorene is greatly larger than that of graphene and is similar to those of the MoS_2 and WSe_2 (1.2–1.8 eV), making this material suitable for various electronic devices. [6, 7, 9, 13] In addition, the direct and thickness-dependent bandgap of phosphorene has attracted further interest because most other 2D semiconductors have indirect band gaps.[17, 18] Castellanos-Gomez highlighted the importance of phosphorene by comparing the bandgap values of different semiconductors.[19] As illustrated in Figure 1-2, the most attractive feature of phosphorene is its exceptional degree of bandgap tunability. Clearly, such high degree of bandgap tunability was not observed for any of other 2D layered materials isolated till now. Therefore, phosphorene can even act as a bridge between graphene and transition metallic dichalcogenides (TMDs) in terms of its band structure. By benefiting from its special band structure, phosphorene could be of potential use in a diverse range of applications including those shown at the bottom of Figure 1-2.

Although recent studies on BP show promising results in a wide range of applications,[10-12] the real success of phosphorene for practical applications will rely significantly on finding a reliable and reproducible method of production. Simple, low-cost and reliable production of phosphorene with superior properties is vitally important for future applications.

1.1.3. Synthesis

The preparation of atomically thin 2D materials is classified into two main approaches: “bottom-up methods” (*e.g.* chemical vapour deposition (CVD) and wet-chemical) and “top-down methods” (mechanical and liquid exfoliation etc.). The layered 2D materials have strong in-plane covalent bonding and weak inter-plane van der Waals interactions, which make these sheets readily separatable from each other. A very well-known example of these 2D materials is graphite which is a layered planar structure consisting of weakly stacked graphene layers.[20] For the production of phosphorene sheets, bottom-up method is not well documented due the experimental limitations and material’s issues. On the other hand, the top-down

method is typically used and exfoliates bulk BP into single- or few-layer phosphorene sheets by applying driving forces to break the weak van der Waals interaction between the stacked layers.

Mechanical cleavage using a scotch-tape method was used for the first demonstration of various 2D materials including phosphorene.[6, 7] In 2014, two independent research groups reported the successful exfoliation of bulk BP flakes into phosphorene nanosheets using scotch tapes.[6, 7] The layer number of phosphorene is one of the most critical parameters that can be used to define its electronic and optical properties. Lu et al.[21] introduced a method that combines traditional mechanical exfoliation and plasma assisted treatment to produce monolayer phosphorene. Moreover they authors showed a reliable way to determine the layer numbers of the phosphorene based on Raman peak intensity. Furthermore, Gomez et al.[22] developed a modified version of the mechanical exfoliation method that has the potential to optimize the yield of FL-BP flakes.

Instability of mechanically exfoliated FL-BP sheets in ambient air is the major drawback that restricts practical use of this material in device applications. It is well known that the lack of stability leads to bubble-like features on the flakes after sample is exposed to air.[8] This issue has led to considerable efforts focused on the development of strategies to protect the phosphorene sheets from degradation. The passivation of phosphorene flakes with protective coatings is promising way to improve the stability.[23-25] For example, Pei et al.[23] produced air-stable phosphorene using layer-by-layer thinning of a phosphorene flake by O_2 plasma etching and further passivation with Al_2O_3. The P_xO_y layer prepared based on the O_2 plasma was not sufficiently robust for successful passivation (see Figure 1-3a), while further passivation using Al_2O_3 showed outstanding stability under ambient conditions (see Figure 1-3b).

Even though mechanically exfoliation has been widely used to prepare phosphorene nanosheets from the bulk BP flakes,[8-10] the labor intensive nature of this method limits its commercial application. Other limitations including lack of control of shape, size and thickness and instability in ambient conditions are the main drawbacks of mechanical exfoliation method. Interestingly, the growth of amorphous BP films on graphene/copper or SiO_2/Si substrates using a pulsed laser deposition

(PLD) method was recently reported.[26] A 2 nm thick amorphous BP based FET device was achieve (Figure 1-3c and d).

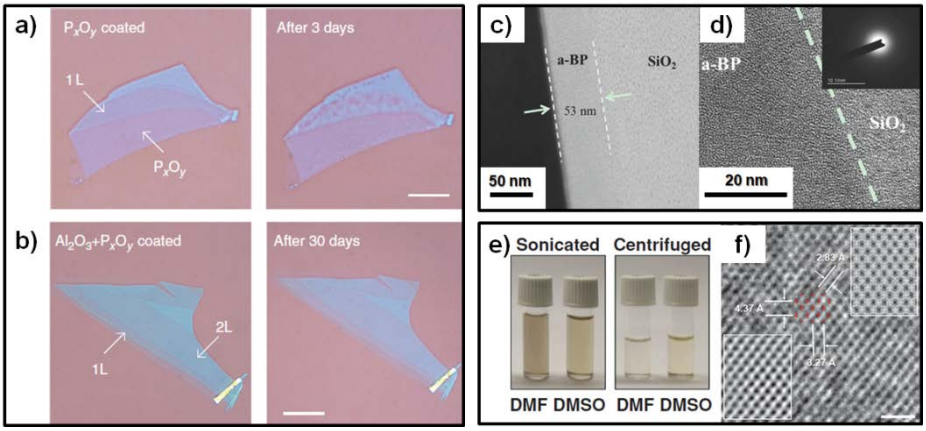

Figure 1-3. Optical microscope images of P_xO_y layer coated mechanically exfoliated phosphorene (a) without and (b) with Al_2O_3 passivation layer.[23] (c) Cross-sectional TEM and (d) HR-TEM image with selected area electron diffraction pattern (inset) of BP thin films prepared using PLD.[26] (e) Photograph and (f) HR-TEM of phosphorene prepared in DMSO and DMF using ultrasonicaton.[29]

Liquid-phase exfoliation (LPE) is a very promising method to prepare 2D layered materials and has many advantages such as scalability and solution processability.[27] The most commonly adopted LPE to prepare 2D nanosheets is based on ultrasonication of bulk crystals in common solvents. The first report producing FL-BP sheets using this method was by Brent et al.[28], who used N-methyl-2-pyrrolidone (NMP) as a solvent. The sonication process was carried out using bath ultrasonication for 24 h. Further, Yasaei et al.[29] also successfully prepared uniform and stable dispersions of phosphorene sheets in both dimethylformamide (DMF) and dimethyl sulfoxide (DMSO) (Figure 1-3e and f).

Phosphorene suffers from serious instability in common solvents (like water, ethanol etc.) due to the presence of oxidizing agents.[8] For this reason, BP should be exfoliated in anhydrous and oxygen-free solvents including NMP, DMF, DMSO, N-cyclohexyl-2-pyrrolidone (CHP) and isopropyl alcohol (IPA). Interestingly, Hersam's group prepared aqueous FL-BP dispersions based on surfactant-assisted LPE and post-processing in deoxygenated water.[30] The results of steps in the

experimental procedure for obtaining water based phosphorene dispersion are illustrated in Figure 1-4. The key for this successful demonstration of phosphorene production was the use of stabilizing surfactants (SDS) in deoxygenated water.

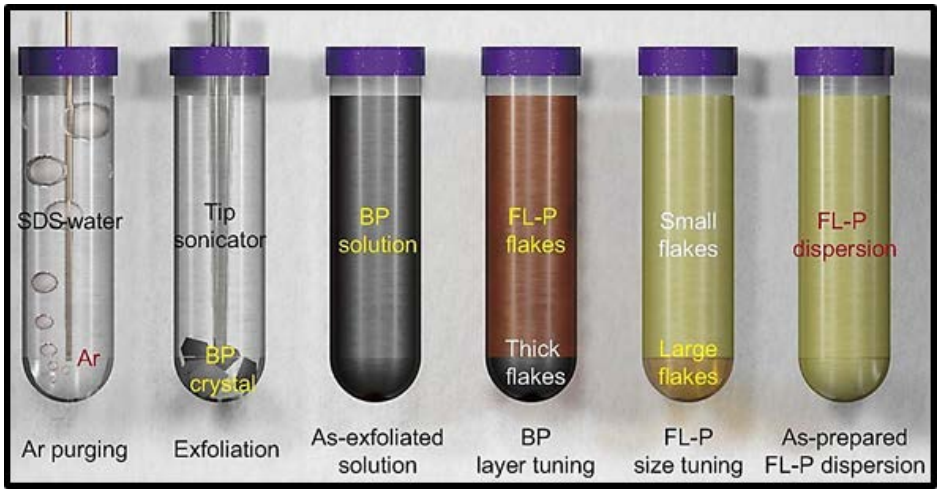

Figure 1-4. Results of the steps in the preparation for aqueous phosphorene dispersions.[30]

Although sonication based LPE is a well-established effective method to prepare solution processable phosphorene, long processing times (>15 h) are required to efficiently separate the bulk BP flakes into individual or FL-BP sheets.[28-30] Additionally such long sonication times are known to reduce the lateral size and create anomalous structural defects in the sheets.[31] The lack of simple, fast and efficient experimental procedures to produce high-quality phosphorene limits its application in different fields.

1.1.4. Application

Increasing energy demand and limited energy resources are the driving forces for the investigation of new energy-harvesting systems. Solar cells - devices that convert solar energy into electricity - are renewable sources of energy that are sustainable and totally inexhaustible. Currently crystalline silicon solar cells make up ~90% of commercial production at present and they can deliver power with approximately 20% efficiency, but they suffer from high manufacturing, installation, and material

costs.[32] Therefore there is currently great interest in developing high efficiency PV devices at low-cost. Emerging PV technologies based on excitonic semiconducting materials, dye sensitizers, organic compounds, perovskite crystals, heterojunction interfaces and quantum dots have drawn increasing attention in the past few decades and are now sitting in the spotlight due to their low-cost, high efficiency and suitability to many more applications than conventional silicon cells.[33] However, many of these cells have some shortcomings that need to be addressed.

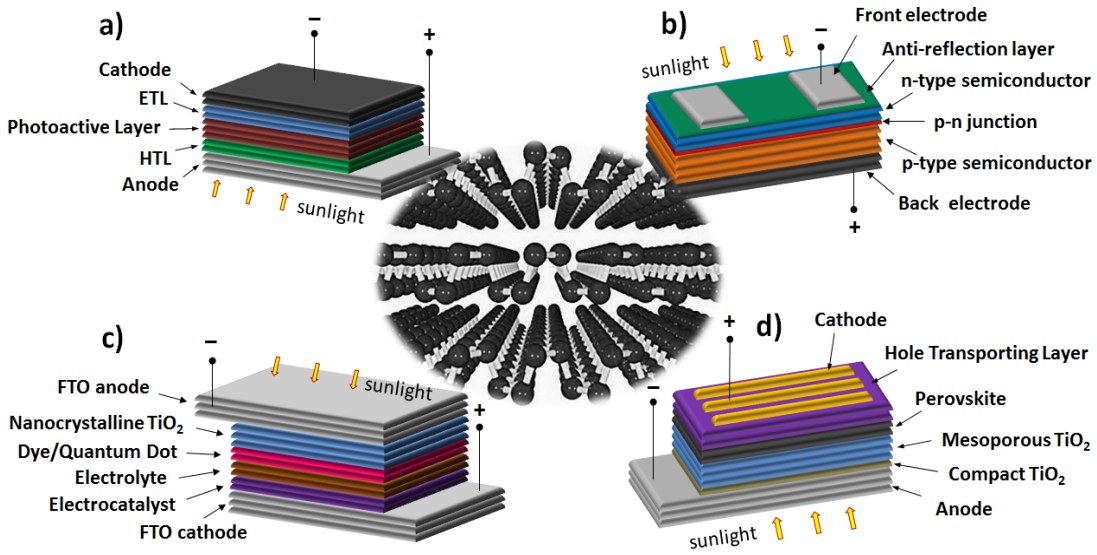

Figure 1-5. The layered structure of (a) organic photovoltaicl (OPV), (b) *p–n* heterojunction solar cell (HJSC), (c) dye and/or quantum-dot sensitized solar cells (DSSC and QDSSC) and (d) perovskite solar cell (PSC). Structure of phosphorene is shown in the middle.[8]

Fascinating properties of phosphorene together with its unique structure make this material an ideal candidate among the burgeoning family of 2D materials for application in many devices including emerging solar cells (Figure 1-5). Research on phosphorene and phosphorene based materials is just few years old. Despite this, outstanding progress in the theoretical and experimental studies of phosphorene has been made to introduce this exciting material into a wide range of applications.[8] In addition to solar cells, phosphorene and phosphorene based materials have already found applications in field-effect-transistors (FETs), batteries, memory devices, supercapacitors, water-splitting devices and sensors. Since the discovery of

phosphorene, there have been an increasing number of theoretical studies on phosphorene for PV applications. In addition to these computational investigations, some exciting developments have been reported on the experimental use of BP derivatives for emerging solar cells over the past few years. Table 1-2 summarizes the previous theoretical and experimental works on the BP derivatives incorporated PV devices.

Table 1-2. Previous works on the use of BP derivatives in emerging solar cells.

Device structure	Cell type	Function	PCE (%)	Type of study, (ref)
AA-/AB-stacked bilayer phosphorene/monolayer MoS_2	HJSC	Heterojunction interface	18	Theory, (ref. 34)
α–AsP/GaN bilayer XSCs	XSC	Electron donor	22.1	Theory, (ref. 35)
Edge-modified phosphorene flakes	HJSC	Donor and Acceptor	20.0	Theory, (ref. 36)
Monolayer phosphorene/$MoTe_2$	XSC	Heterojunction interface	12.0	Theory, (ref. 37)
$MoSe_2$/Ψ-phosphorene	HJSC	Heterojunction interface	20.26	Theory, (ref. 38)
phosphorene/MoS_2	HJSC	Heterojunction interface	17.5	Theory, (ref. 39)
ITO/ZnO/FL-BP/ PTB7:PC71BM/MoO_3/Ag	OPV	ETL	8.25	Experiment, (ref. 40)
FTO/TiO_2/Dye/Electrolyte/BP QDs-PANI/FTO	DSSC	Counter electrode	6.85	Experiment, (ref. 41)
ITO/ZnO/BP-PCBM/PEDOT:PSS/Ag	HJSC	Heterojunction interface	8.30	Experiment, (ref. 42)
ITO/PEDOT/BPQDs/CH_3NH_3 PbI_3/PCBM/Ag	PSC	HTL	16.69	Experiment, (ref. 43)

To fabricate high performance PV devices with phosphorene sheets, matching the energy levels of the cell components with phosphorene is of great importance. Electron and hole transfer process must be energetically favourable. The energy levels of the phosphorene (1-5 layers) are plotted and compared with the most commonly used components of emeging solar cells in Figure 1-6. Highly tunable conduction and valence bands of the phosphorene offer the advantage of energy level matching with other components in these classes of solar cells. The ambipolar conduction, tunable energy level and unique structure of phosphorene would allow it to be used in either an anode or a cathode of solar cells.

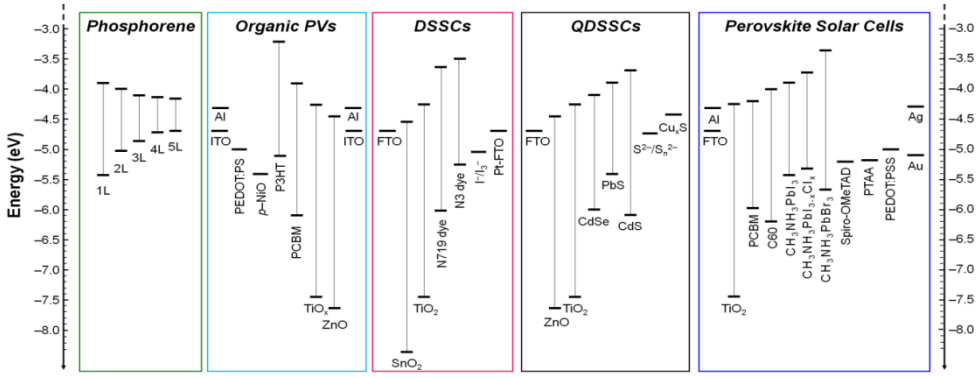

Figure 1-6. Energy level diagram of phosphorene and commonly used materials in OPVs, DSSCs, QDSSCs and PSCs. The conduction band and valence band values of phosphorene are taken from ref. [44]. Figure is reproduced from ref. [8].

Despite the fact that excellent progress has been made on the use of phosphorene in some of these emerging solar cells in the past, a lot still remains to be done in this field. So far, the BP derivatives such as nanosheets and QDs have been employed in OPVs,[40] DSSCs,[41] HJSCs,[42] and PSCs[43].

As one type of emerging PV devices, carbon nanotube-silicon (CNT-Si) solar cells are a promising PV system and have attracted considerable research interest from the PV community over the past decade.[45, 46] CNT-Si solar cells show the outstanding optoelectronic properties of CNTs combined with high optical absorption of Si.[45-48] Moreover these HJSCs, compared with traditional Si solar panels, promise to be less expensive and easier to fabricate. Impressive progress has been done in this class of solar cells in the past.[46]

In particular, single-walled CNTs (SWCNTs) are commonly used to fabricate high efficiency solar cells due to their tunable energy levels matching a wide range of the solar spectrum and high charge transport properties.[49] In a typical SWCNT-Si solar cell, a transparent SWCNT film is placed on the surface of a moderately doped *n*-type Si (*n*-Si) substrate.[46] Upon illumination, photons are transmitted through the SWCNT film and absorbed by the Si, which leads to the creation of electron and hole pairs. After migrating into the depletion region at the junction, these pairs are then separated into free charge carriers under the effect of a built-in potential across the heterojunction at the interface (see Figure 1-7).[46] Finally the electrons and holes are collected at the Si and SWCNT film, respectively.

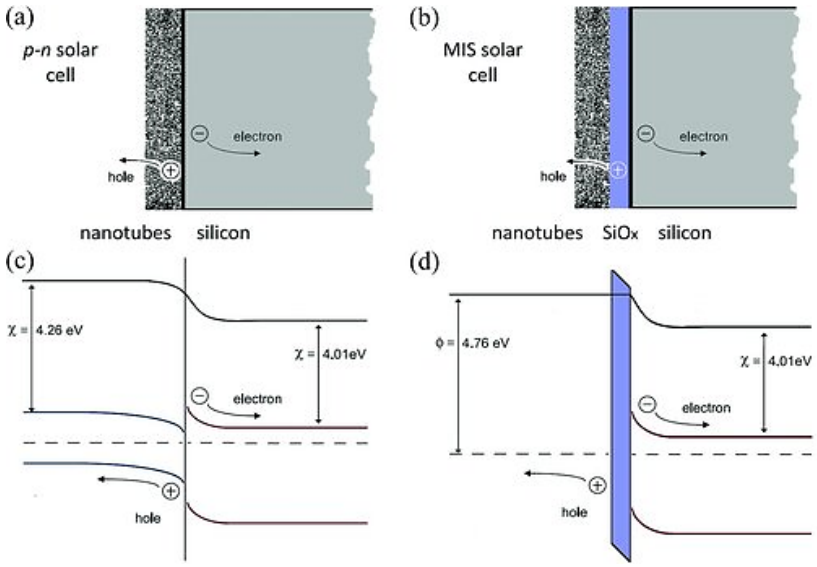

Figure 1-7. Device schematics and energy diagrams for (a,c) p-n heterojunction and (b,d) metal-insulator-semiconductor (MIS) solar cells.[46]

In the standard SWCNT-Si solar cells, the PV efficiencies are fundamentally limited because of the sparse network and poor hole selectivity of SWCNTs. In order to address these issues, a large number of efforts have been made incorporating ultrathin 2D nanoflakes such as graphene oxide (GO) and graphene, additional hole conducting materials and conductive polymers in the SWCNT films.[50-53] Even though 2D nanosheets can improve the SWCNT network (nanotube junction) and provide a better contact with the substrate,[50, 51] the poor hole selectivity of these systems still remains to be an issue. On the other hand, the use of organic hole

transporting[50] and conductive polymer interlayers[53] has shown to enhance the hole selectivity of the devices and thus increased the power conversion efficiency (PCE). However, the integration of these hole selective materials cannot satisfy the requirement of dense networking of SWCNTs for the solar cells.

Interestingly, FL-BP and/or phosphorene sheets are an ultrathin 2D structures and exhibit *p*-type dominated conduction characteristics. Therefore it is reasonable to expect that the incorporation of phosphorene sheets into the SWCNT films will simultaneously address both the network and hole selectivity issues of SWCNT-Si solar cells.

1.2. Aims and Objectives

This Thesis aims to investigate the possibility of solution proccesable synthesis of few-layer black phosphorus (FL-BP) sheets using MW-assisted technique and their applicability in single-walled carbon nanotube-silicon (SWCNT-Si) heterojunction solar cells. As such, the following objectives were set for this thesis:

(a) Producing high-quality FL-BP sheets using a facile, novel, efficient and extremely fast method based on MW-assisted liquid-phase exfoliation method (LPE).

(b) Comparing the FL-BP products prepared from our MW-exfoliation and ultrasonication based exfoliation methods.

(c) Understanding the fundamental features of FL-BP flakes produced using MW-assisted LPE

(d) Exploring the effect of FL-BP flakes on the photovoltaic performance of SWCNT-Si solar cells.

(e) Fabricating highly efficiency FL-BP–SWCNT-Si solar cells.

(f) Investigating the internal mechanism of SWCNT-Si solar cells with and without FL-BP flakes using density-functional theory (DFT) calculation.

1.3. Thesis Outline

The outline of the thesis is described as follows:

Chapter 1 provides an overview of the research topics (black phosphorus and solar cells) studied in this Master's project, aims, objectives and outline of the thesis.

Chapter 2 describes detailed experimental procedures to prepare all samples and solar cells reported in this thesis.

Chapter 3 presents results obtained from this project and provides some important discussions. The results of the MW-exfoliated few-layer black phosphorus sheets are presented and compared with the nanosheets prepared with conventional sonication based method. Furthermore, the photovoltaic results obtained using the fabricated solar cell devices are also presented in this chapter.

Chapter 4 summarizes the research that have been carried out and reported in this thesis and highlights some important future directions in this research field.

Appendix A includes information about the computational (density-functional theory (DFT) calculation) details.

1.4. References

[1] K. S. Novoselov, A. K. Geim, S. V. Morozov, D. Jiang, Y. Zhang, S. V. Dubonos, I. V. Grigorieva, A. A. Firsov, *Science*, **2004**, *306*, 666.

[2] A. K. Geim, K. S. Novoselov, *Nat Mater*, **2007**, *6*, 183.

[3] H. Zhang, *ACS Nano*, **2015**, *9*, 9451.

[4] M. Chhowalla, Z. Liu, H. Zhang, *Chem. Soc. Rev*, **2015**, *44*, 2584.

[5] M. Chhowalla, H. S. Shin, G. Eda, L.-J. Li, K. P. Loh, H. Zhang, *Nat Chem*, **2013**, *5*, 263.

[6] L. Li, Y. Yu, G. J. Ye, Q. Ge, X. Ou, H. Wu, D. Feng, X. H. Chen, Y. Zhang, *Nat Nanotechnol*, **2014**, *9*, 372.

[7] H. Liu, A. T. Neal, Z. Zhu, Z. Luo, X. Xu, D. Tománek, P. D. Ye, *ACS Nano*, **2014**, *8*, 4033.

[8] M. Batmunkh, M. Bat-Erdene, J. Shapter, *Adv. Mater*, **2016**, *28*, 8586.

[9] L. Kou, C. Chen, S. C. Smith, *J. Phys. Chem. Lett*, **2015**, *6*, 2794.

[10] R. Xu, J. Yang, Y. W. Myint, J. Pei, H. Yan, F. Wang, Y. Lu, *Adv. Mater*, **2016**, *28*, 3493.

[11] G. Zhao, T. Wang, Y. Shao, Y. Wu, B. Huang, X. Hao, *Small*, **2017**, *13*, 1602243.

[12] J. Wu, N. Mao, L. Xie, H. Xu, J. Zhang, *Angew. Chem Int. Ed*, **2015**, *54*, 2366.
[13] F. Xia, H. Wang, Y. Jia, *Nat Commun*, **2014**, *5*, 4458.
[14] J. He, D. He, Y. Wang, Q. Cui, M. Z. Bellus, H.-Y. Chiu, H. Zhao, *ACS Nano*, **2015**, *9*, 6436.
[15] M. Z. Rahman, C. W. Kwong, K. Davey, S. Z. Qiao, *Energy Environ. Sci*, **2016**, *9*, 709.
[16] R. Fei, L. Yang, *Nano Lett*, **2014**, *14*, 2884.
[17] A. H. Woomer, T. W. Farnsworth, J. Hu, R. A. Wells, C. L. Donley, S. C. Warren, *ACS Nano*, **2015**, *9*, 8869.
[18] Y. Jing, Q. Tang, P. He, Z. Zhou, P. Shen, *Nanotechnology*, **2015**, *26*, 095201.
[19] A. Castellanos-Gomez, *J. Phys. Chem. Lett*, **2015**, *6*, 4280.
[20] O. Hod, *J Chem Theory Comput*, **2012**, *8*, 1360.
[21] W. Lu, H. Nan, J. Hong, Y. Chen, C. Zhu, Z. Liang, X. Ma, Z. Ni, C. Jin, Z. Zhang, *Nano Res*, **2014**, *7*, 853.
[22] C.-G. Andres, V. Leonardo, P. Elsa, O. I. Joshua, K. L. Narasimha-Acharya, I. B. Sofya, J. G. Dirk, B. Michele, A. S. Gary, J. V. Alvarez, W. Z. Henny, J. J. Palacios, S. J. v. d. Z. Herre, *2D Materials*, **2014**, *1*, 025001.
[23] J. Pei, X. Gai, J. Yang, X. Wang, Z. Yu, D.-Y. Choi, B. Luther-Davies, Y. Lu, *Nat Commun*, **2016**, *7*, 10450.
[24] B. Wan, B. Yang, Y. Wang, J. Zhang, Z. Zeng, Z. Liu, W. Wang, *Nanotechnology*, **2015**, *26*, 435702.
[25] H. Uk Lee, S. C. Lee, J. Won, B.-C. Son, S. Choi, Y. Kim, S. Y. Park, H.-S. Kim, Y.-C. Lee, J. Lee, *Sci. Rep*, **2015**, *5*, 8691.
[26] Z. Yang, J. Hao, S. Yuan, S. Lin, H. M. Yau, J. Dai, S. P. Lau, *Adv. Mater*, **2015**, *27*, 3748.
[27] L. Niu, J. N. Coleman, H. Zhang, H. Shin, M. Chhowalla, Z. Zheng, *Small*, **2016**, *12*, 272.
[28] J. R. Brent, N. Savjani, E. A. Lewis, S. J. Haigh, D. J. Lewis, P. O'Brien, *Chem. Comm*, **2014**, *50*, 13338.
[29] P. Yasaei, B. Kumar, T. Foroozan, C. Wang, M. Asadi, D. Tuschel, J. E. Indacochea, R. F. Klie, A. Salehi-Khojin, *Adv. Mater*, **2015**, *27*, 1887.
[30] J. Kang, S. A. Wells, J. D. Wood, J.-H. Lee, X. Liu, C. R. Ryder, J. Zhu, J. R. Guest, C. A. Husko, M. C. Hersam, *Proc. Natl. Acad. Sci*, **2016**, *113*, 11688.
[31] M. Batmunkh, C. J. Shearer, M. J. Biggs, J. G. Shapter, *J. Mater. Chem. A*, **2016**, *4*, 2605.
[32] M. Batmunkh, M. J. Biggs, J. G. Shapter, *Small*, **2015**, *11*, 2963.
[33] M. Jacoby, *Chem Eng News*, **2016**, *94*, 30.
[34] J. Dai, X. C. Zeng, *J. Phys. Chem. Lett*, **2014**, *5*, 1289.
[35] M. Xie, S. Zhang, B. Cai, Y. Huang, Y. Zou, B. Guo, Y. Gu, H. Zeng, *Nano Energy*, **2016**, *28*, 433.
[36] W. Hu, L. Lin, C. Yang, J. Dai, J. Yang, *Nano Lett*, **2016**, *16*, 1675.

[37] V. D. S. O. Ganesan, J. Linghu, C. Zhang, Y. P. Feng, *Appl. Phys. Lett*, **2016**, *108*, 122105.
[38] H. Wang, X. Li, Z. Liu, J. Yang, *Phys. Chem. Chem. Phys*, **2017**, *19*, 2402.
[39] H. Guo, N. Lu, J. Dai, X. Wu, X. C. Zeng, *J. Phys. Chem. C*, **2014**, *118*, 14051.
[40] S. Lin, S. Liu, Z. Yang, Y. Li, T. W. Ng, Z. Xu, Q. Bao, J. Hao, C.-S. Lee, C. Surya, F. Yan, S. P. Lau, *Adv. Funct. Mater*, **2016**, *26*, 864.
[41] Y. Yang, J. Gao, Z. Zhang, S. Xiao, H.-H. Xie, Z.-B. Sun, J.-H. Wang, C.-H. Zhou, Y.-W. Wang, X.-Y. Guo, P. K. Chu, X.-F. Yu, *Adv. Mater*, **2016**, *28*, 8937.
[42] L. Bai, L. Sun, Y. Wang, Z. Liu, Q. Gao, H. Xiang, H. Xie, Y. Zhao, *J. Mater. Chem. A*, **2017**, *5*, 8280.
[43] W. Chen, K. Li, Y. Wang, X. Feng, Z. Liao, Q. Su, X. Lin, Z. He, *J. Phys. Chem. Lett*, **2017**, *8*, 591.
[44] Y. Cai, G. Zhang, Y.-W. Zhang, *Sci. Rep*, **2014**, *4*, 6677.
[45] D. D. Tune, J. G. Shapter, *Energy Environ. Sci*, **2013**, 6, 2572.
[46] D. D. Tune, B. S. Flavel, R. Krupke, J. G. Shapter, *Adv. Energy Mater*, **2012**, 2, 1043.
[47] W. Xu, S. Wu, X. Li, M. Zou, L. Yang, Z. Zhang, J. Wei, S. Hu, Y. Li, A. Cao, *Adv. Energy Mater*, **2016**, 6, 1600095.
[48] X. Li, Z. Lv, H. Zhu, *Adv. Mater*, **2015**, 27, 6549.
[49] Y. Jung, X. Li, N. K. Rajan, A. D. Taylor, M. A. Reed, *Nano Lett*, **2013**, *13*, 95.
[50] L. Yu, M. Batmunkh, T. Grace, M. Dadkhah, C. Shearer, J. Shapter, *J. Mater. Chem. A*, **2017**, *5*, 8624.
[51] W. Xu, B. Deng, E. Shi, S. Wu, M. Zou, L. Yang, J. Wei, H. Peng, A. Cao, *ACS Appl. Mater. Interfaces*, **2015**, *7*, 17088.
[52] L. Yu, D. Tune, C. Shearer, J. Shapter, *ChemSusChem*, **2015**, *8*, 2940.
[53] L. Yu, D. D. Tune, C. J. Shearer, J. G. Shapter, *ChemNanoMat*, **2015**, *1*, 115.

Chapter 2.

Experimental Details

2.1. Materials

BP (99.998% pure) was obtained from Smart Elements. Arc-discharge SWCNTs (P3-SWNT) were purchased from Carbon Solution Inc., Riverside, CA, USA. Unless otherwise stated, all chemicals were purchased from Sigma-Aldrich Co., Ltd., Australia and used as received.

2.2. Preparation of FL-BP

The MW-assisted technique based LPE method (See Figure 2-1) includes two-step microwaving processes using two different types of MW instruments. The first MW (StartSYNTH Microwave Synthesis Labsta-tion, Milestone s.r.l) was operating with 600 W power and set temperature of 50 ^{o}C. The second MW was carried out using CEM Discover SP – MW operating with a power of 220 W and set temperature of 70 ^{o}C.

Firstly, 25 mg of bulk BP was immersed in 5 mL of NMP. The BP-NMP mixture was heated using the first MW (termed “MW-1”) for different periods of time (4 min to 20 min), followed by treatment with the second MW (termed “MW-2”) for 3 min. Then, a supernatant (~4 mL) was taken and centrifuged at 6000 rpm for 30 min. After centrifugation, the top 70% of the solution was collected for further analysis and application. Finally, the stable dispersion of FL-BP flakes was obtained after centrifugation.

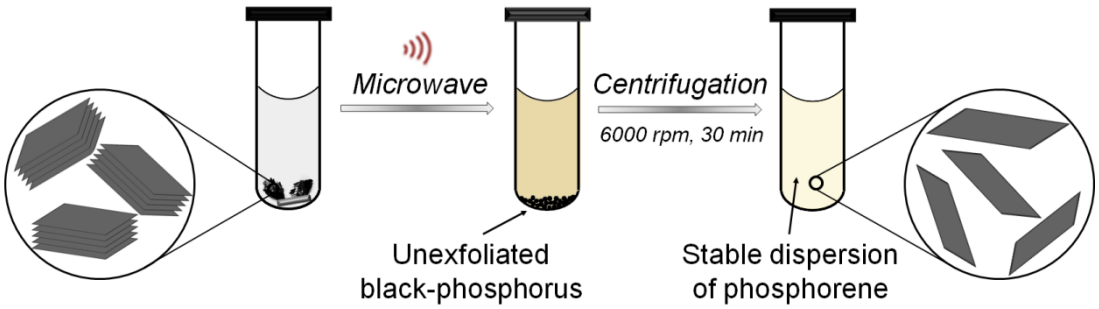

Figure 2-1. Schematic for MW-assisted LPE of bulk BP flakes to produce FL-BP solutions.

For comparison, FL-BP flakes were also prepared using ultrasonication based LPE. Typically, the BP-NMP or BP-CHP mixture (25 mg in 5 mL) was sonicated using bath ultrasonication (Elma, Germany) for 24 h. During the sonication, the temperature was controlled at around 30 ^{o}C by adding ice. After the exfoliation, the samples were subject to centrifugation at 6000 rpm for 30 min. Finally the top 60% of the solution was collected for further analysis.

2.3. Preparation of SWCNT suspension

5 mg of arc-discharge SWCNTs (P3-SWNT, Carbon solutions) were bath sonicated in 50 mL Triton X-100 based aqueous solution (1% *v*/*v*) solution for 1 h at room temperature. During the sonication, the temperature was maintained below 35^{o}C. The suspension was centrifuged at 17,500 g for 1 h. Then the bottom residue was discarded and the supernatant was then centrifuged in the same manner as the previous one. The second supernatant was collected and used as the stock suspension.

2.4. Preparation of FL-BP–SWCNT solution and films

To prepare the FL-BP and SWCNT composite, different volumes of aqueous SWCNT suspensions (0.5, 1.0, 1.5, 2.0 and 2.5 mL) were mixed with the corresponding volumes of NMP with and without FL-BP flakes (0.5, 1.0, 1.5, 2.0 and 2.5 mL). The prepared suspensions were further diluted with DI water to 250 mL in total. Notably, to explore the effect of only FL-BP on the PV performance of SWCNT-Si solar cells, our control SWCNT-Si devices (reference cells) were fabricated with the addition of NMP. The films were prepared by vacuum filtration of the previously prepared solutions. The diluted suspension was collected onto a mixed cellulose ester (MCE) membrane (0.45 μm, HAWP, Millipore) under the support of a nitrocellulose ‘stencil’ membrane (25 nm, VSWP, Millipore) (see Figure 2-2 for detail). After the filtration, the films were rinsed with water to remove any remaining residue.

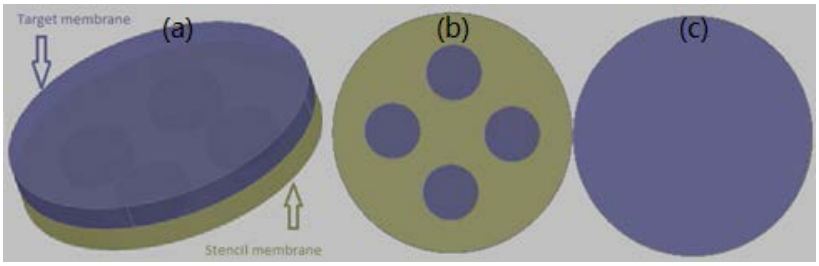

Figure 2-2. (a) 3D structure, (b) bottom and (c) top view of "target" (0.45 μm) and 'stencil' (0.25 nm) membrane. There are 4 holes on 'stencil' membrane (green). Materials are collected on target membrane (purple).

2.5. Device fabrication

Solar cells were fabricated on *n*-type Si wafers (5–10 Ω cm, 525 mm thick with a 100 nm thermal oxide, ABC GmbH, Germany). Positive photoresist (AZ1518, micro resist technology GmbH, Germany) was coated onto the Si wafers at 3000 rpm for 30 s, followed by drying at 100°C for 60 s. A mask was placed on top of the surface and an active area (0.079 cm^2) was defined by exposing the masked substrate to UV-light (3 min). Then the wafer was immersed in a basic developer solution (AZ 326 MIF, AZ Electronic Materials GmbH, Germany) for 60 s to develop the photoresist. After rinsing with water and drying under a nitrogen gas, the Cr/Au (5/145 nm) front electrode was coated by a dual target sputter coater (Quorumtech, Q300T-D) with a quartz crystal microbalance. To dissolve the photoresist, the substrate was then immersed in acetone for 60 min followed by mild sonication for 60 s. A buffered oxide etch (6:1 of 40% NH_4F and 49% HF) was applied to the active area for ~90 s to remove the top 100 nm.

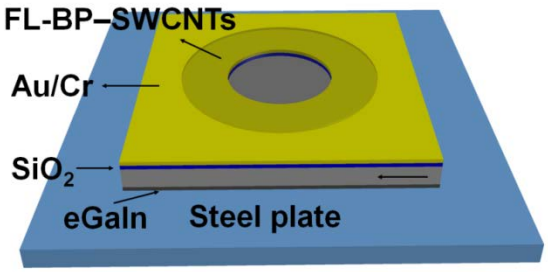

Figure 2-3. Schematic of SWCNT-Si solar cell employing FL-BP sheets.

Then the previously prepared films (membranes with SWCNT-only, SWCNT-NMP and FL-BP–SWCNT) were placed onto the substrates with SWCNT or FL-BP–SWCNT side down. A water droplet was dropped onto wet the membrane for better adhesion between the film and substrate. The assembled devices were clamped and baked for ~20 min at 80°C in an oven. After cooling to room temperature, acetone was used to remove the MCE membrane and to wash (30 min for 3 times). Then the rear oxide layers were etched. The devices were completed with gallium indium eutectic (eGaIn) back contacts and mounted on steel plates (see Figure 2-3). Upon completion of this process, three well-established post-treatments were applied to all devices.[1-4]

2.5.1. Post treatment

The as-prepared devices have undergone three well-established chemical treatments using HF, $SOCl_2$ and HF.[1-4] First of all, an HF (2 %) treatment was used to etch the oxide layer which was formed on top of Si surface during the cell fabrication. This was carried out by putting 1 drop on top of the device for 10 s and then rinsing with water and ethanol. To measure the transmittance and sheet resistance (R_{sheet}), the films were placed on microscope slides.We note that since HF can react with glass and ruin the sample, it was replaced by HCl in the same manner for these samples. $SOCl_2$ treatment was conducted by dropping 2 drops of $SOCl_2$ onto the surface of the cells/films, followed by rinsing with ethanol and drying with N_2. The second HF treatment was carried out in the same manner as the first HF treatment in order to etch the oxide layer induced by $SOCl_2$ treatment and observe the effect of $SOCl_2$ treatment.

2.6. Characterization and measurement

2.6.1. Device testing

The photocurrent-voltage (*J-V*) characteristics of the devices were analyzed using a Keithley 2400 SMU instrument and recorded using a custom LabView Virtual Instrument program. An example J-V curve and its important PV parameters such as short-circuit current (J_{sc}), open-circuit voltage (V_{oc}), fill factor (FF) and power conversion efficiency (PCE) are shown in Figure 2-4. A standard Si test cell with

NIST-traceable certification was used to calibrate the power density as 100 mW cm^{-2} at the sample plane of the collimated a 150W xenon-arc light source (Newport), which was passed through an AM 1.5G filter. The cells were tested under both light and dark conditions to estimate the efficiency and the diode properties. The active area of the devices was 0.079 cm^2. The devices were tested in air using the reverse-scan direction from +1 to -1 V. No device preconditioning, such as prolonged light soaking or forward voltage bias, and no equilibration time was used. External quantum efficiency (EQE) spectra ranging from 300 to 1100 nm were recorded by passing chopped light from a xenon source through a monochromator and onto the devices. The light intensity of the illumination source was adjusted using a photodiode detector (silicon calibrated detector, Newport). The transmittances of the films on glass substrates were measured using a Varian Cary 50G UV–vis spectrophotometer at wavelengths ranging from 400 to 800 nm. R_{sheet} measurements were performed on the same films using a four-point probe technique (KeithLink Technology Co., Ltd. Taiwan).

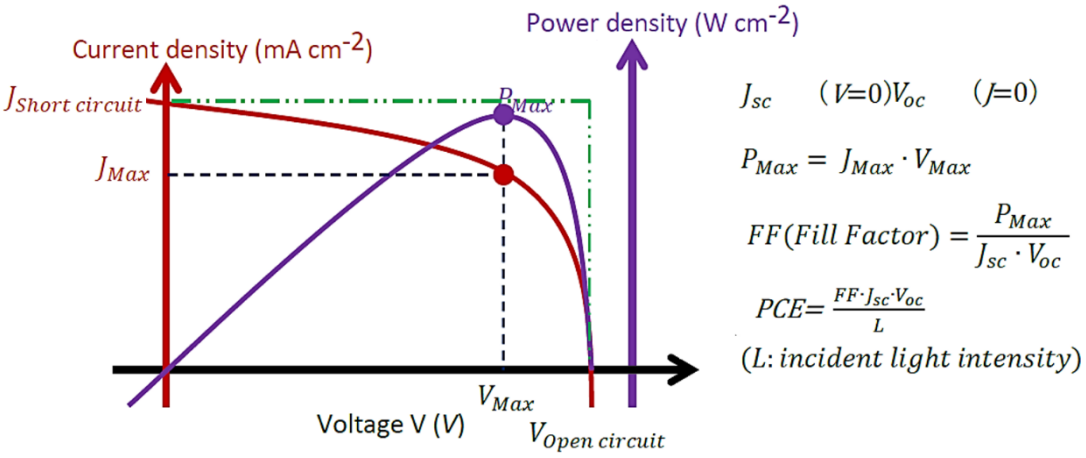

Figure 2-4. Example of photocurrent-voltage (J-V) curve of solar cell and its important PV parameters such as J_{sc} ($J_{short\ circuit}$), V_{oc} ($V_{open\ circuit}$), FF and PCE.

2.6.2. Materials characterization

The optical absorption of the samples was analyzed using a UV-vis-NIR spectroscopy (Perkin Elmer Lambda 950) at wavelengths ranging from 200 nm to 2200 nm. Notably, the optical absorption measurements were carried out after the

subtraction of MW-treated NMP solvent as the background. For instance, for the optical absorption of 11 min MW-exfoliated FL-BP solution, the background solvent (NMP) only was treated using MW technique for 11 min and used for the background subtraction.

Atomic force microscopy (AFM) was performed in air using either a Bruker Dimension FastScan AFM with Nanoscope V controller, operating in Peak Force Tapping mode or a Bruker multimode AFM with Nanoscope V controller, operating in standard tapping mode. Peakforce tapping mode images were acquired using Bruker ScanAsyst-air probes (nominal tip diameter and spring constant is 4 nm and 0.4 N/m respectively) and for tapping mode the probes used were silicon HQNSC15/AlBS Mikromasch probes (nominal tip diameter and spring constant is 16 nm and 40 N/m respectively). Set-point, scan rate and gain values were chosen to optimize image quality and flake thickness using procedures outlined by Shearer et al.[5] for Peakforce tapping mode and Nemes-Incze[6] for standard tapping mode. The AFM topography images have been flattened and thickness measurements were made using the section analysis tool of Nanoscope Analysis 1.4. For AFM analysis, the samples were prepared by spin coating the as-prepared solutions onto cleaned silicon substrates at 3000 rpm for 20 s. Scanning electron microscopy (SEM) images were obtained using an Inspect F50 SEM (FEI) with accelerating voltage of 5.0 kV.

Raman spectra were acquired using a Witec alpha300R Raman microscope at an excitation laser wavelength of 532 nm with a 40x objective (numerical aperture 0.60). Typical integration times for single Raman spectra were between 30-60 s for 2-3 accumulations. Confocal Raman images were also acquired with integrations between 1 to 6 seconds per pixel. Each pixel in the Raman images represents a Raman spectrum with the number of pixels in a typical Raman image representing hundreds of spectra. Confocal Raman images are generated by plotting the intensity of a specified region of each Raman spectrum that corresponds to a material, versus the X-Y position of the excitation laser as it scans the sample surface. The highest resolution grating available on the instrument with 1800 grooves mm^{-1} was used . This grating has a spectral resolution of ~1 wavenumber which is insufficient to resolve the peak shifts expected for four layers or less phosphorene compared to BP as has been noted by numerous research groups.[7-9] Laser power levels were kept as

low as possible to prevent sample damage.[10] The power was approximately 1 mW or below.

Auger electron spectroscopy (AES) (including elemental mapping) and simultaneous Secondary Electron Microscopy was performed on a PHI710 Scanning Auger Nanoprobe. The vacuum pressure in the analysis chamber during analysis was maintained at approximately 10^{-10} Torr. A 10 kV electron beam with a beam current of 10 nA was used to produce SEM images and AES data. Elemental maps were obtained at either 512 x 512 or 256 x 256 pixel resolution. Bright-field transmission electron microscopy (TEM) images were acquired using a FEI Titan Themis at 80kV accelerating voltage. Samples were dispersed by drop-casting onto quantifoil SQR12-200CU grids at 80°C in air for ~2 mins until dry, and then immediately transferred to high vacuum storage prior to analysis.

2.7. References

[1] D. D. Tune, B. S. Flavel, R. Krupke, J. G. Shapter, *Adv. Energy Mater*, **2012**, *2*, 1043.

[2] L. Yu, D. Tune, C. Shearer, J. Shapter, *ChemSusChem*, **2015**, *8*, 2940.

[3] L. Yu, D. D. Tune, C. J. Shearer, J. G. Shapter, *ChemNanoMat*, **2015**, *1*, 115.

[4] D. D. Tune, J. G. Shapter, *Nanomaterials*, **2013**, *3*, 655.

[5] C. J. Shearer, A. D. Slattery, A. J. Stapleton, J. G. Shapter, C. T. Gibson, *Nanotechnology*, **2016**, *27*, 125704.

[6] P. Nemes-Incze, Z. Osváth, K. Kamarás, L. P. Biró, *Carbon*, **2008**, *46*, 1435.

[7] C.-G. Andres, V. Leonardo, P. Elsa, O. I. Joshua, K. L. Narasimha-Acharya, I. B. Sofya, J. G. Dirk, B. Michele, A. S. Gary, J. V. Alvarez, W. Z. Henny, J. J. Palacios, S. J. v. d. Z. Herre, *2D Materials*, **2014**, *1*, 025001.

[8] A. Favron, E. Gaufres, F. Fossard, A.-L. Phaneuf-Lheureux, N. Y. W. Tang, P. L. Levesque, A. Loiseau, R. Leonelli, S. Francoeur, R. Martel, *Nat Mater*, **2015**, *14*, 826.

[9] W. Lu, H. Nan, J. Hong, Y. Chen, C. Zhu, Z. Liang, X. Ma, Z. Ni, C. Jin, Z. Zhang, *Nano Res*, **2014**, *7*, 853.

[10] I. Calizo, A. A. Balandin, W. Bao, F. Miao, C. N. Lau, *Nano Lett*, **2007**, *7*, 2645.

Chapter 3.

Results and Discussion

3.1. Production of FL-BP flakes

3.1.1. Optical characteristics

In order to find the best experimental condition to prepare high quality FL-BP flakes, we first focused on optimizing the parameters such as temperature and processing times of the MW instruments. For the "MW–1", we found 50 ^{o}C is the optimum parameter to efficiently exfoliate the BP among a range from 50 ^{o}C to 120 ^{o}C (Figure 3-1a). We also found that the combination of "MW–1" and "MW–2" is very effective in producing high-yield, FL-BP solution (Figure 3-1b). The mechanism of MW-exfoliation and other shear-exfoliation methods for 2D materials has been well described elsewhere.[1-3] Briefly, when MW irradiation is applied to the sample, the van der Waals interactions between the bulk BP flakes starts weakening and further exfoliates layer by layer in the appropriate solvent.

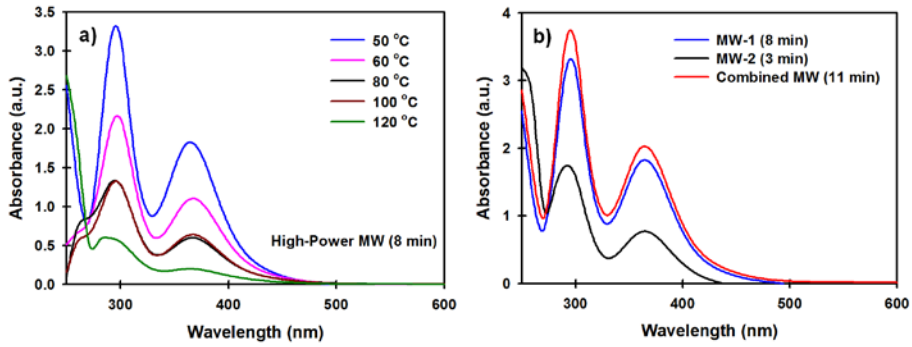

Figure 3-1. UV-vis spectra of FL-BP in NMP prepared using (a) "MW-1" only at different temperatures for 8 min, and (b) MW-1 (8 min), MW-2 (3 min) and their combination.

The FL-BP dispersions were prepared by exfoliating bulk BP for different exfoliation times in "MW–1", always followed by the "MW–2" for 3 min. For comparison, bulk BP was exfoliated in NMP using bath sonication for 24 h. Figure 3-2 shows photographs of FL-BP dispersions obtained for different MW-exfoliation times. The dispersion color for 11 min MW-exfoliation is much clear than the other dispersions, indicating more efficient exfoliation and higher yield of FL-BP. Our FL-BP dispersion obtained by sonication showed a cloudy pale yellow or turbid color (Figure 3-3). As compared to the sonicated solution, a much clear yellow color of

FL-BP dispersion prepared using MW-exfoliation suggests the production of high-quality FL-BP in NMP. However, as the MW time increases to 15 min, the yellow color started to disappear probably due to sample damage and NMP decomposition.

This work points the way forward to reduce the processing time to make high-quality FL-BP from many hours to a few minutes. Considerable experiments are still required to explore the microwave parameters (time, power, temperature, etc.) to give the optimal yield of phosphorene. It may of course be that one set of conditions will give the largest amount of FL-BP while other conditions will be best to give single layer samples.

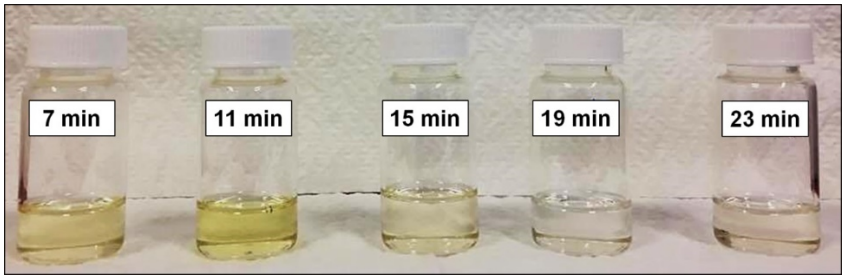

Figure 3-2. Photographs of FL-BP solutions in NMP prepared by exfoliating bulk BP using different MW-exfoliation times

Figure 3-3. Photograph of FL-BP in NMP prepared by exfoliating bulk BP using ultrasonication for 24 h.

Figure 3-4a shows the optical absorption (in the NIR range) spectra of NMP-based FL-BP solutions prepared using different MW-times. For comparison, the absorption spectrum of the FL-BP dispersion prepared by the sonication for 24 hr is depicted in the inset of Figure 3-4a. Several spectral peaks were observed at around 1.38, 1.23,

1.05, 0.86, 0.72 and 0.64 eV (labelled 1-6) which can be associated with the fundamental bandgap values in 1 to 6 layers of phosphorene, respectively.[4] These peak energies are consistent with photoluminescence (PL) peaks reported for 1 to 5 layers of mechanically exfoliated BP.[5, 6] The smaller peak intensities at 1.38, 1.23 and 1.05 eV compared to other peaks indicate that the yields of 1 to 3 atomic layers of phosphorene are lower than other layers. The yield of the 4 and 5 layer MW-exfoliated BP flakes was comparable to that prepared using sonication based LPE.

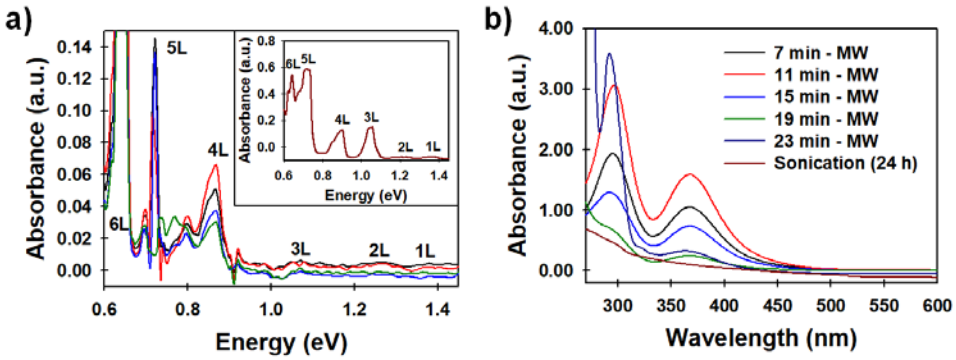

Figure 3-4. (a) NIR and (b) UV-vis spectra of FL-BP solutions prepared by different MW-exfoliation times. The inset shows the spectrum of the FL-BP solution prepared by 24 h sonication.

Based on the peak intensity at 0.867 eV (assigned to be due to 4 layers of phosphorene in the literature), one can see that the FL-BP dispersion prepared using 11 min MW-exfoliation exhibited the highest absorbance (Figure 3-4a), indicating better yield of few layer phosphorene. Short MW-exfoliation times were found to be insufficient, while long MW times seem to damage the samples. For instance, after the exfoliation for 7 min, the large BP sheets were found to start separating and a limited yield of FL-BP was obtained (see Figure 3-5a). Therefore such short processing time is insufficient to separate the BP layers into single or few layers. However, the absorption spectrum in the NIR (Figure 3-5b) for a long MW time (23 min) showed negative peaks. We believe that this is due to sample damage producing small phosphorene pieces (see SEM images in Figure 3-5). Moreover, Zhu et al.[2] found that short processing time (using kitchen blender) can produce nanosheets, but when longer processing time is used, the BP sheets disappeared and resulting in

ultrasmall black phosphorus quantum dots (BPQDs). This finding is similar to what we observed from our samples when long MW processing time is used (Figure 3-5d).

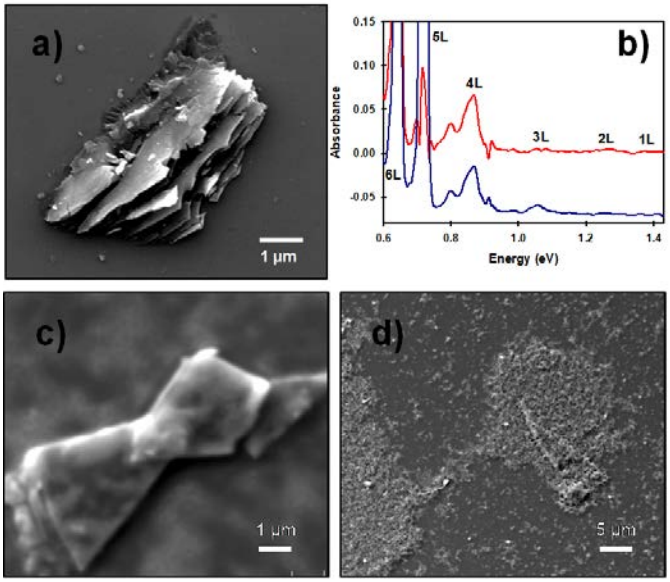

Figure 3-5. (a) SEM image of MW-exfoliated BP in NMP for 7 min. (b) Optical absorption spectra of FL-BP solutions (red for 11 min and blue for 23 min) in the NIR region. SEM image of BP flakes after MW treatment of (c) 11 min and (d) 23 min.

The FL-BP solutions were further characterized using UV-vis spectroscopy (Figure 3-4b). Two main absorption peaks at around 300 and 370 nm were observed for all samples, which are consistent with previous results obtained from both the theoretical[7] and experimental investigations[8, 9]. Interestingly, the peak of our MW-exfoliated BP solutions at 370 nm was very strong and sharp as compared to that of the FL-BP dispersion prepared by sonication based exfoliation in this work (Figure 3-4b) and reported in previous studies.[8, 9] This strong and sharp peaks may indicate that our FL-BP sheets prepared using MW-exfoliation are very high-quality. Therefore, based on the absorption spectra of our samples across the NIR and UV-vis (Figure 3-6), we focused on the 11 min MW-exfoliated BP for further analysis.

Ahmed et al.[10] reported the UV-vis spectrum of mechanically exfoliated phosphorene layer, which was very consistent with our UV-vis spectra of FL-BP exhibiting two major peaks at around 300 nm and 370 nm. We also note that to the

best of our knowledge, except our MW-exfoliated FL-BP, no experimental work on solution processed phosphorene has previously shown these three major peaks which are predicted by theory.

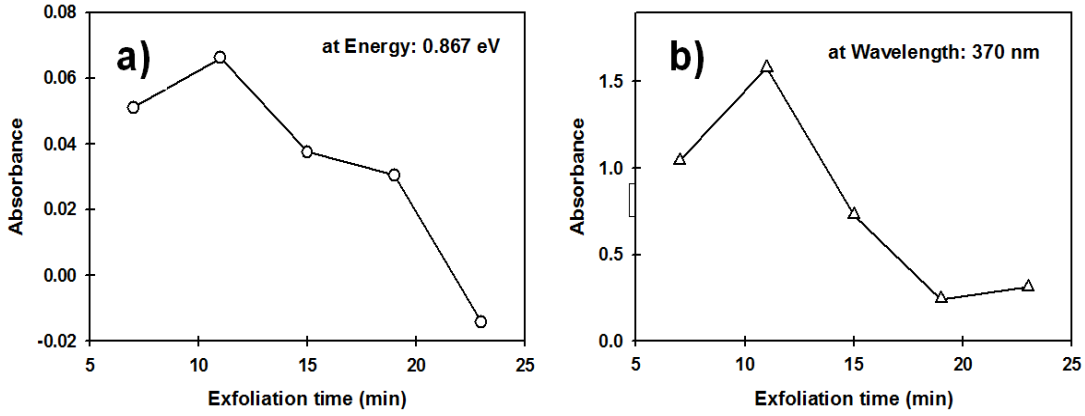

Figure 3-6. Optical absorption of FL-BP solutions prepared using different MW-exfoliation times at the wavelength of (a) 1430 nm (NIR range, 4 L peak) and (b) 370 nm (UV-vis range).

3.1.2. Microscopic characteristics

According to previous atomic force microscopy (AFM) studies,[11, 12] the thickness of single layer phosphorene is ~0.85 nm, which is slightly higher than that of the theoretical value (~0.6 nm)[11 13]. We have plotted a histogram of heights of our MW-exfoliated FL-BP flakes taken from more than 200 measurements (see Figure 3-7). The AFM images used to analyse the average height profile measurements are depicted in Figure 3-8. These results show that the measured heights of our FL-BP flakes vary from ~ 2 nm to ~15 nm, verifying that our sample consists of few-layer to multilayer (2–18 layers) sheets. In line with the NIR results, yield of 2 layer phosphorene was low compared to few-layer (4-6). When 2 layers are observed, they were typically situated at the edges of thicker flakes (Figure 3-8a). Based on the AFM height measurements in Figure 3-7, we find the average thickness for all the flakes analyzed equal to 6.5 ± 2.6 nm. This yields a range of layer numbers from 4 to 11 layers while the range of layer numbers for the ultrasonicated sample was 4 to 6 (Figure 3-9).

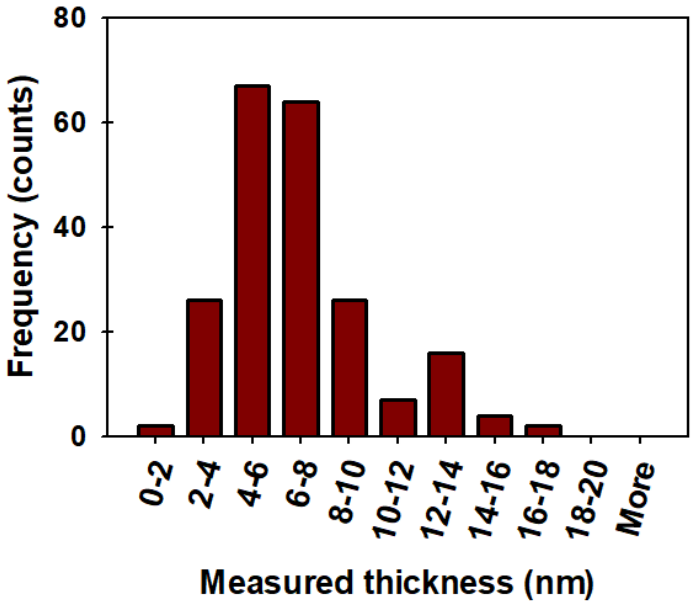

Figure 3-7. Histogram of heights taken from more than 200 AFM measurements.

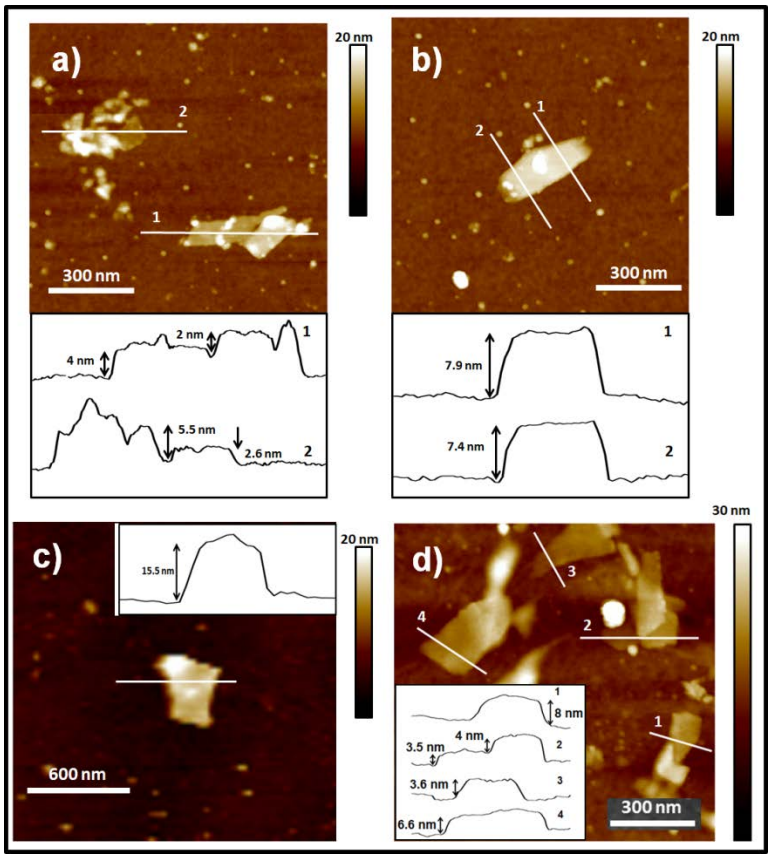

Figure 3-8. AFM images of MW-exfoliated FL-BP.

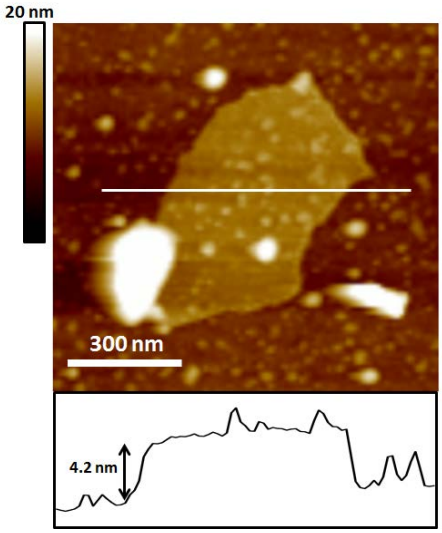

Figure 3-9. AFM image and corresponding height measurement of FL-BP sheet prepared using ultrasonication based LPE. The average thickness of bath sonicated FL-BP flake was 4.5 ± 0.7 nm (from 16 measurements), which is 4 to 6 layers.

The lateral size distribution of our FL-BP flakes was investigated using SEM. As shown in Figure 3-10a-c, the lateral dimensions of our FL-BP ranged from hundreds of nanometers up to ~4 µm.

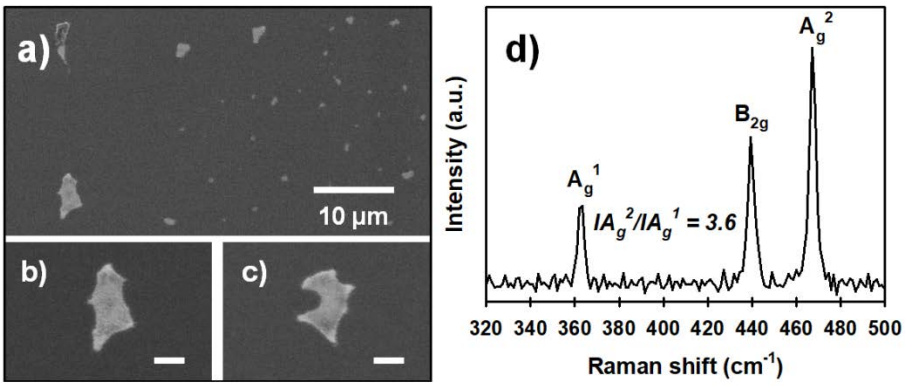

Figure 3-10. (c-e) SEM images and (f) Raman spectrum of FL-BP sheets. Scale bars in (d) and (e) are 2.0 µm.

A Raman spectrum of our FL-BP flakes produced using MW-assisted LPE is depicted in Figure 3-10d. The Raman modes centered at 362.2 cm^{-1}, 439.4 cm^{-1} and 467.3 cm^{-1} can be assigned to the characteristic of A_g^1, B_{2g} and A_g^2 phonon modes,

respectively, and are in agreement with the signature Raman spectrum of the phosphorene.[11, 12] However, compared to our bulk BP (Figure 3-11), no significant shift and change in the Raman spectrum was observed after 11 min MW-assisted exfoliation. Favron et al.[13] showed that there are no noticeable shifts in the three vibrational modes of the bulk BP where the phosphorene has more than four layers.

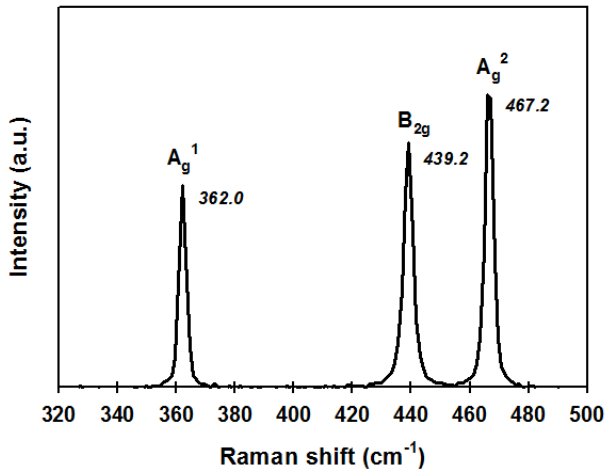

Figure 3-11. Raman spectrum of the bulk BP before the exfoliation.

The ratio of the area under the peaks for the A_g^2 and A_g^1 bands can be used to determine the layer number of phosphorene sheets.[12, 13] Lu et al.[12] found that the A_g^2/A_g^1 ratio changed from 1.9 for bulk BP to 3.5 for 3 layers and increased to 10.5 for single layer. The A_g^2/A_g^1 integrated intensity ratio for the Raman spectra in Figure 3-10d is 3.6 suggesting 3 layers BP for this region. By mapping the A_g^2/A_g^1 ratio across a flake, approximate layer number over that flake can be determined. The Raman images in Figure 3-12(i) and (ii) show the intensity maps of a flake for the A_g^2 peak and A_g^1 peaks, respectively, while the data in Figure 3-12(iii) is a map of the A_g^2/A_g^1 integrated intensity ratio. The A_g^2/A_g^1 ratio varies from ~2 to ~4 across the flake, indicating the flake ranges from 3 to 5 layers at its thinnest region which is consistent with data from AFM and absorption spectra. Moreover, a signature for the degradation and/or oxidation of phosphorene from Raman spectrum is the emergence of a broad feature in the region under the B_{2g} and A_g^2 modes,[13] which is not observed in our sample demonstrating the structural integrity.

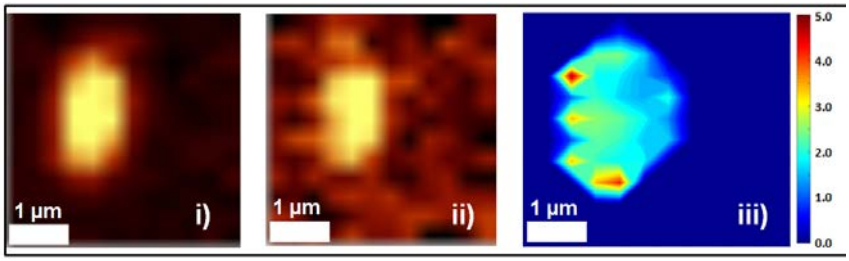

Figure 3-12. Confocal Raman images for the A_g^2 peak (i), A_g^1 peak ii) and A_g^2/A_g^1 (iii) ratio of the same flake.

Scanning Auger microscopy can determine elemental composition with high spatial resolution as it combines SEM with Auger electron spectroscopy (AES). Figure 3-13a-d shows that the FL-BP flake under analysis has large lateral dimensions from 2 to 4 µm, which is consistent with the sizes observed in the SEM images. The elemental mapping in Figure 3-13a-d indicates that our FL-BP sample on silicon substrate consists of three different elements, namely P, C and O.

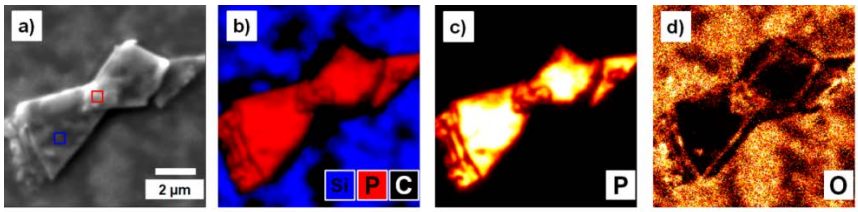

Figure 3-13. Auger elemental mapping and spectrum of FL-BP flake. (a) SEM image showing where the Auger maps were obtained. (b) Si (blue), P (red) and C (black) mapping, (c) P mapping and (d) O mapping.

Figure 3-14 shows the AES spectra for two locations on the flake shown in Figure 3-13a. Interestingly, the Auger spectrum obtained at the center of the flake showed only single "P" element (non-oxidized), while the edge of the flakes was partially oxidized (see Figure 3-13d). It has been reported that the oxidation starts to occur on the phosphorene from the edges of the flakes when exposed to air.[13, 14] The stability and degradation of FL-BP is the major challenge in phosphorene research and needs to be addressed with a great sense of urgency.

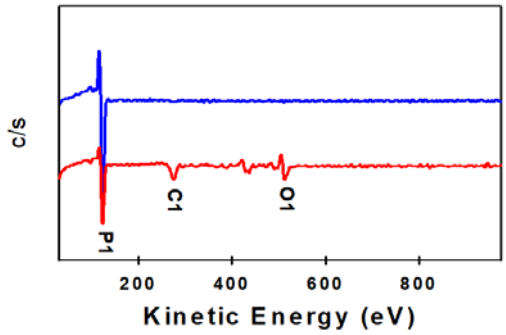

Figure 3-14. The elemental spectrum corresponding to the two different locations (blue and red) as shown in Figure 3-13a.

Figure 3-15 shows the transmission electron microscopy (TEM) images of our FL-BP sheets. The majority of the sheets look transparent, indicating that they are ultrathin and are only few-layers. The lateral sizes of the sheets were quite non-uniform, which further confirms that the MW-assisted LPE of bulk BP produces FL-BP sheets with the lateral sizes ranging from hundreds of nanometers to micron-scale. Selected area electron diffraction (SAED) (see Figure 3-15a inset) was used to confirm the high-quality, single-crystal structure of our FL-BP. Therefore the results are in excellent agreement with previous reports.[15, 16] High-resolution TEM (HRTEM) of our FL-BP in Figure 3-15b displays its atomic structure, where the lattice spacing was ~0.27 nm, which is consistent with the previously reported values of single-layer and few-layer phosphorene.[16]

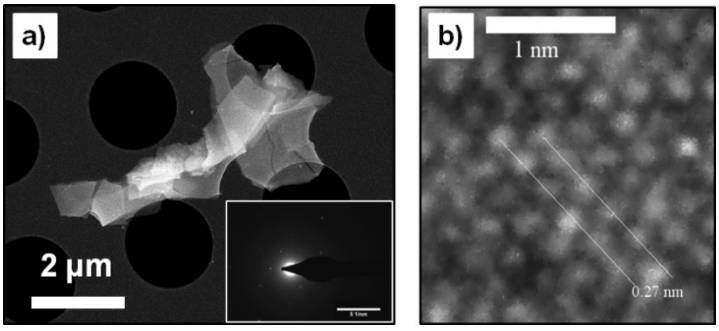

Figure 3-15. (a) TEM image of our FL-BP sheets produced using MW-assisted LPE. Inset shows the SAED pattern of the FL-BP. (b) HRTEM image of FL-BP nanoflake taken from a selected area in (a).

3.2. FL-BP–SWCNTs composite

Figure 3-16a shows an SEM image of SWCNTs before incorporating the FL-BP flakes, confirming the absence of flakes over a large-area taken with low-resolution SEM. In order to prepare the FL-BP–SWCNTs composite, an appropriate volume of NMP based FL-BP solution was added into the aqueous SWCNT suspension. Figure 3-16b depicts an SEM image of the FL-BP–SWCNTs composite. Clearly, bundles of SWCNTs are wrapped around the FL-BP flake (~1.5 µm in lateral size), indicating successful integration of the FL-BP flakes into the SWCNTs.

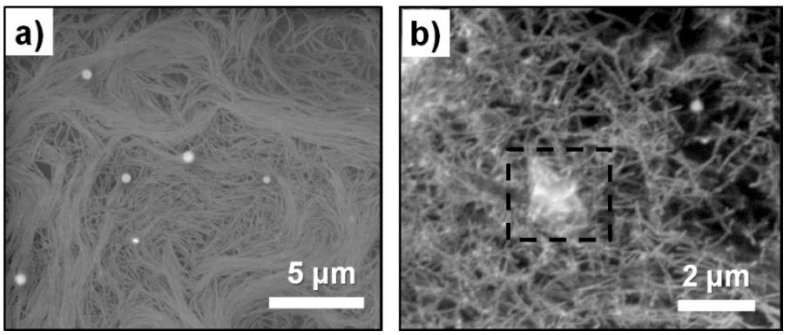

Figure 3-16. (a) SEM image of SWCNTs (a) without and (b) with FL-BP flakes. Black box indicates the existence of FL-BP flake in the SWCNT network. 1 mL CNTs and 1 mL FL-BP were mixed to prepare the composite.

To further confirm the presence of FL-BP flakes in the composite, the sample was analyzed using Raman spectroscopy. As shown in Figure 3-17, the Raman spectrum of the composite contains all the characteristic peaks for both SWCNTs and phosphorene including the radial breathing mode (RBM) (at ~175 cm^{-1}), "D" band (at ~1346 cm^{-1}), "G" band (at ~1591 cm^{-1}) and "G'" band (at ~2675 cm^{-1}) of SWCNTs, and A_g^1 mode (at ~362 cm^{-1}), B_{2g} mode (at ~439 cm^{-1}) and A_g^2 mode (at ~465 cm^{-1}) of phosphorene (see Figure 3-17 inset). It is well understood that phosphorene suffers from poor stability in ambient conditions and common solvents such as water. Despite this, our FL-BP flakes exfoliated in NMP still remain stable when mixed with water based SWCNT suspension.

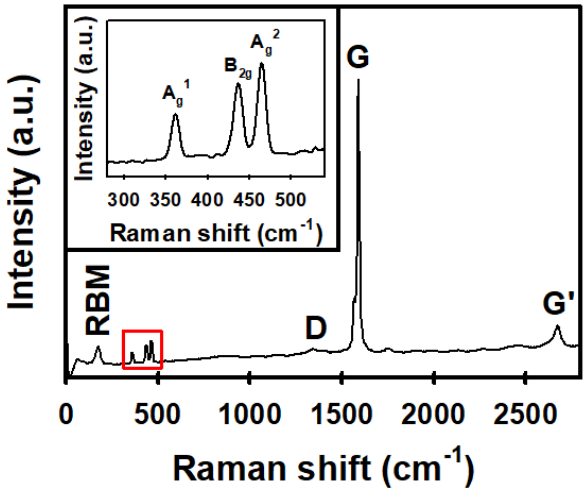

Figure 3-17. Raman spectrum of FL-BP and SWCNT composite. Inset: Zoom into the region of the Raman spectrum of FL-BP peaks in the composite. 1 mL CNTs and 1 mL FL-BP were mixed to prepare the composite.

3.3. Photovoltaic characterization

A vacuum filtration method was used to prepare SWCNT films with and without FL-BP flakes for device fabrications.[17] Since the FL-BP flakes were prepared in NMP solvent, we added an appropriate volume of NMP solvent into the SWCNT suspension before the filtration for our control cells. By doing this, we were able to explore the influence of only FL-BP on the PV characteristics of SWCNT-Si solar cells. Once cell fabrication was completed, all films and/or cells have undergone three chemical post treatments using HF, $SOCl_2$ and HF. In order to understand the effect of these chemical treatments on the FL-BP, only FL-BP-Si solar cells were fabricated and treated in the same manner using these three treatments. Based on the result (see Figure 3-18), we confirm that these treatments do not influence the FL-BP for this class of solar cells.

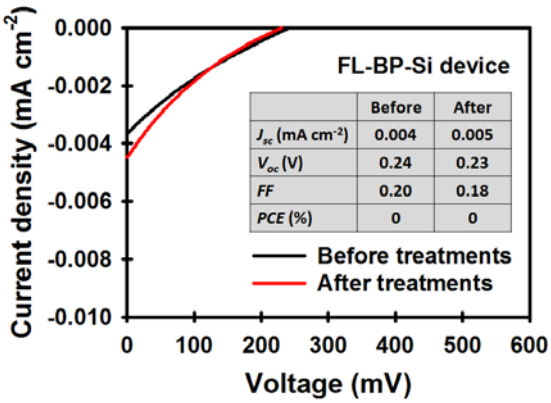

Figure 3-18. PV characteristics of FL-BP-Si solar cell before and after treatments.

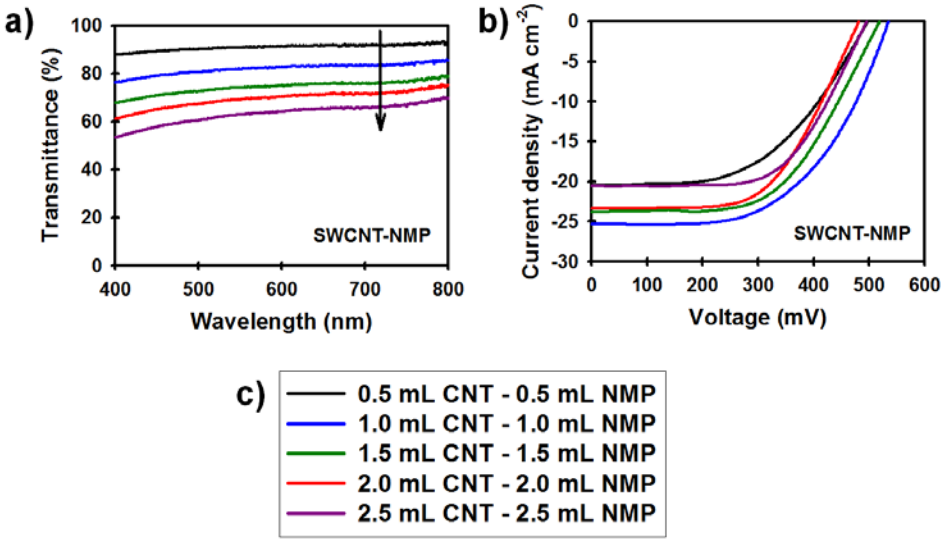

Figure 3-19. (a) Optical transmittance, (b) J–V curves and (c) sample labelling of five different thicknesses of SWCNT-NMP based films and solar cells.

An ideal solar cell is achieved by having the lowest possible R_{sheet} at the highest possible transparency of the CNT film. Clearly there is a trade-off between the conductivity and transparency of the films depending on the thickness. The thickness of our films was controlled by changing the volume of filtered solution. The optical transparencies of five different thicknesses of SWCNT films (NMP added) are depicted in Figure 3-19a. Clearly, the transmittance of the films decreased with increasing filtered volume of the SWCNT solution as expected.

Table 3-1. PV parameters of five different thicknesses of SWCNT-Si solar cells (NMP added). Average values and the standard deviations are calculated based on at least three cells. The best cells are highlighted in bold.

Device	J_{sc}; (mA cm^{-2})	V_{oc}; (V)	FF	PCE; (%)	T; (%)	R_{sheet}; (Ω)
0.5 mL CNT– 0.5 mL NMP	**20.44**; 20.66 ± 0.53	**0.490**; 0.492 ± 0.003	**0.52**; 0.51 ± 0.01	**5.28**; 5.13 ± 0.12	90.85	1838 ± 171
1.0 mL CNT– 1.0 mL NMP	**25.31**; 25.06 ± 0.36	**0.552**; 0.543 ± 0.013	**0.56**; 0.52 ± 0.02	**7.52**; 7.35 ± 0.25	81.94	803 ± 24
1.5 mL CNT– 1.5 mL NMP	**23.79**; 23.64 ± 0.21	**0.519**; 0.517 ± 0.003	**0.57**; 0.55 ± 0.02	**6.97**; 6.72 ± 0.35	74.10	457 ± 37
2.0 mL CNT– 2.0 mL NMP	**23.41**; 23.24 ± 0.44	**0.481**; 0.481 ± 0.001	**0.58**; 0.57 ± 0.01	**6.49**; 6.42 ± 0.10	69.18	270 ± 12
2.5 mL CNT– 2.5 mL NMP	**20.56**; 19.76 ± 0.69	**0.495**; 0.493 ± 0.002	**0.60**; 0.61 ± 0.01	**6.16**; 5.93 ± 0.20	62.91	254 ± 13

Figure 3-19b shows the J-V characteristics of the solar cells fabricated with NMP added SWCNT films and their corresponding PV parameters have been summarized in Table 3-1. Due to its high R_{sheet} (~1838 Ω), the device with the highest transparency showed the lowest short-circuit current (J_{sc}) (20.44 mA cm^{-2}) and fill factor (FF) (0.52) as compared to the thicker films based cells. The FF value of our devices continuously increased from 0.51 to 0.61 with increasing the film thickness because of the improved film conductivity (see Table 3-1). Indeed the best PV parameters were achieved for the cells fabricated based on SWCNT films (~803 Ω@81.9% T) prepared from "1 mL CNT – 1 mL NMP". The observed J_{sc}, open-circuit voltage (V_{oc}), and FF values for the best device with this SWCNT film were 25.31 mA cm^{-2}, 0.55 V, and 0.56, respectively, yielding a PCE of 7.52%.

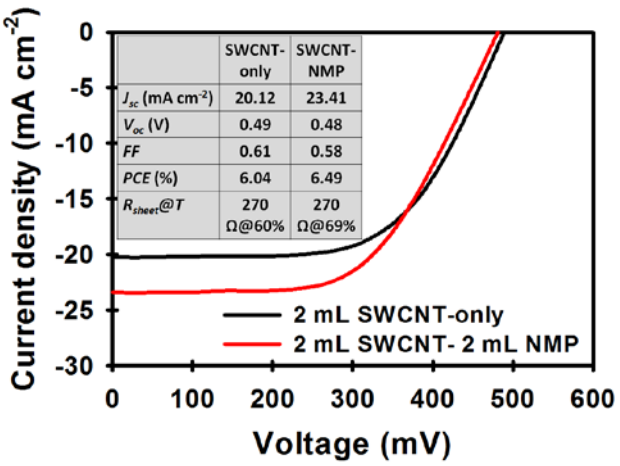

Figure 3-20. PV characteristics of devices fabricated with SWCNT films prepared from SWCNT without and with NMP. The same volume (2 mL) of SWCNT solutions was used for both devices.

For comparison, SWCNT-Si devices were also fabricated using the SWCNT-only suspension without the addition of NMP. A SWCNT-only film (~270 Ω@~60% T) was used for the device fabrication. The SWCNT-Si solar cell prepared using this film exhibited a PCE of 6.04%. The measured J_{sc}, V_{oc} and FF were 20.12 mA cm^{-2}, 0.49 V and 0.61 (Figure 3-20). Interestingly, the cell fabricated based on 2 mL NMP added SWCNT film showed an improved PCE (6.49%) as compared to the device fabricated with SWCNT-only film (6.04%). The increased J_{sc} (from 20.12 mA cm^{-2} to 23.41 mA cm^{-2}) was the key contribution to this PCE enhancement due to the increased improved transparency. Therefore the addition of 2 mL NMP enhanced the transparency of the CNT film (with no change in the R_{sheet}). This enhancement in the transparency may be due to the upgraded dispersion of SWCNTs in water and thus resulted in better film uniformity. Moreover, the NMP may dope the SWCNTs to make them more p-type and hence improve the quality of the heterojunction leading to an improved PCE. Herein we show that the addition of NMP in SWCNT solution can enhance the PCE of the SWCNT-Si cells and obtain a PCE of up to 7.52%.

Compared to the films prepared from NMP added SWCNT, the FL-BP–SWCNT films show reduced transparencies despite the same volume of SWCNT solution being used (Figure 3-21a). This is due to the continuous and dense network formed by introduction of FL-BP into the SWCNT (Figure 3-16b). Interestingly, the R_{sheet} of FL-BP–SWCNT films were higher than those of SWCNTs films at similar

transmittance. For example, the FL-BP–SWCNT film with 82.9% transmittance showed a R_{sheet} of 1166 ± 50 Ω/sq while SWCNT film exhibited a R_{sheet} of 803 ± 24 Ω/sq at ~82% transmittance (Table 3-2). Since the phosphorene is a semiconducting material (not conductor), it is not surprising that the R_{sheet} of the FL-BP–SWCNT film was higher than that of the SWCNT film despite having similar transparency.

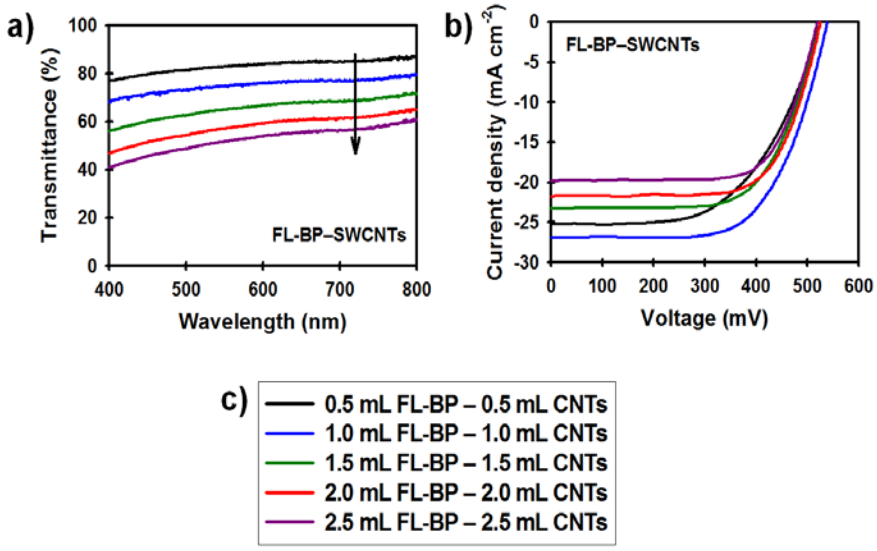

Figure 3-21. (a) Optical transmittance, (b) J–V curves and (c) sample labelling of five different thicknesses of FL-BP–SWCNTs based films and solar cells.

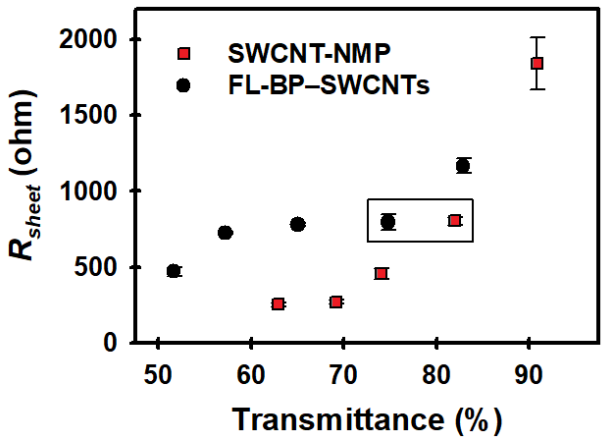

Figure 3-22. R_{sheet} vs Transmittance of different thicknesses of SWCNT-NMP and FL-BP–SWCNT films. Box highlights the properties of the films used for the best-performing devices for each device structure.

Table 3-2. PV parameters of five different thicknesses of FL-BP–SWCNT-Si cells. Average values and the standard deviations are calculated based on at least three cells. The best cells are highlighted in bold.

Device	J_{sc}; (mA cm^{-2})	V_{oc}; (V)	FF	PCE; (%)	T; (%)	R_{sheet}; (Ω)
0.5 mL FL-BP–0.5 mL CNTs	**25.25**; 24.81 ± 0.55	**0.529**; 0.525 ± 0.004	**0.56**; 0.56 ± 0.01	**7.51**; 7.36 ± 0.16	82.91	1166 ± 50
1.0 mL FL-BP–1.0 mL CNTs	**26.90**; 26.70 ± 0.28	**0.538**; 0.538 ± 0.001	**0.65**; 0.64 ± 0.01	**9.37**; 9.20 ± 0.25	74.78	796 ± 53
1.5 mL FL-BP–1.5 mL CNTs	**23.24**; 23.14 ± 0.12	**0.528**; 0.530 ± 0.002	**0.66**; 0.66 ± 0.00	**8.08**; 8.07 ± 0.01	65.04	780 ± 11
2.0 mL FL-BP–2.0 mL CNTs	**21.72**; 21.00 ± 0.76	**0.530**; 0.527 ± 0.003	**0.68**; 0.69 ± 0.01	**7.88**; 7.62 ± 0.27	57.22	726 ± 5.0
2.5 mL FL-BP–2.5 mL CNTs	**19.83**; 19.83 ± 0.10	**0.521**; 0.521 ± 0.003	**0.70**; 0.70 ± 0.00	**7.25**; 7.23 ± 0.02	51.68	471 ± 30

Even though FL-BP–SWCNT films showed lower transparency and higher R_{sheet} than the SWCNT films (see Figure 3-22a), surprisingly the solar cells fabricated using these films exhibited higher PCEs. It was mentioned earlier that the transparency of the film plays an important role in the operation of the devices as it determines the amount of light that reaching the Si. In this regard, although the FL-BP lowers the transparency with little change in the R_{sheet}, the cell performance improves clearly indicating the flakes positively influence the electronic states of the system. These states have been examined based on DFT calculations and will be discussed later in Appendix.

We also attempted to maximize the PV efficiency of our devices by adding different FL-BP loadings in the SWCNT for device fabrication. However, the solar cells prepared based on “1 mL FL-BP + 1 mL SWCNT” were still the best devices, exhibiting the highest efficiency (see Figure 3-23). Furthermore, the best-performing devices of both SWCNT-Si and FL-BP–SWCNT-Si solar cells were selected for

further investigation. The electrical and optical properties of the films are highlighted (black box) in Figure 3-22.

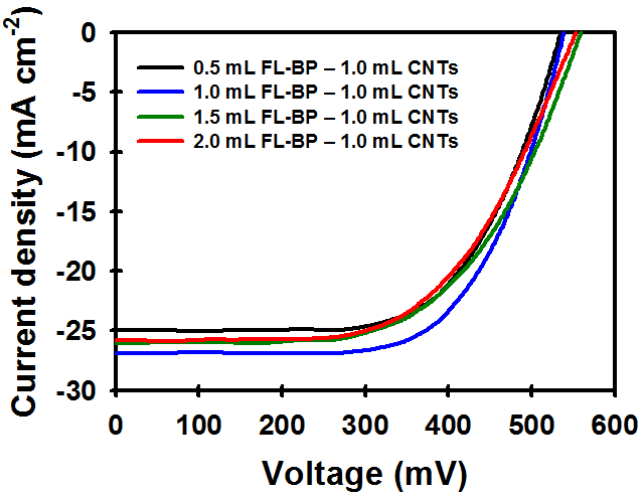

Figure 3-23. J-V curves of the FL-BP–SWCNT-Si solar cells prepared using different FL-BP loadings in the SWCNTs.

Figure 3-24a shows the J-V curves of the best-performing SWCNT-Si and FL-BP–SWCNT-Si solar cells and the corresponding PV parameters have been summarized and compared in Table 3-3. As shown in Table 3-3, the solar cell fabricated with FL-BP flakes exhibited a PCE of 9.37% which was significantly higher than the control cell with SWCNT-NMP film (7.52%). The increased J_{sc} value was one of the key contributing PV parameters to the PCE enhancement of the solar cells. To confirm the J_{sc} enhancement, the incident photon-to-current efficiency (IPCE) or external quantum efficiency (EQE) spectra of the cells were measured (see Figure 3-24b). The device with FL-BP flakes shows a clear improvement in EQE at the wavelengths between 300–800 nm. The J_{sc} was calculated from the IPCE spectrum of each device and J_{sc} difference of the devices was also calculated. The calculated J_{sc} difference (1.75 mA cm^{-2}) of SWCNT-Si and FL-BP–SWCNT-Si devices was consistent with that (1.60 – 1.70 mA cm^{-2}) calculated from the J-V characteristics. This enhancement in the J_{sc} is due to the improved hole selectivity of the SWCNT film by using *p*-type dominated FL-BP sheets.[18]

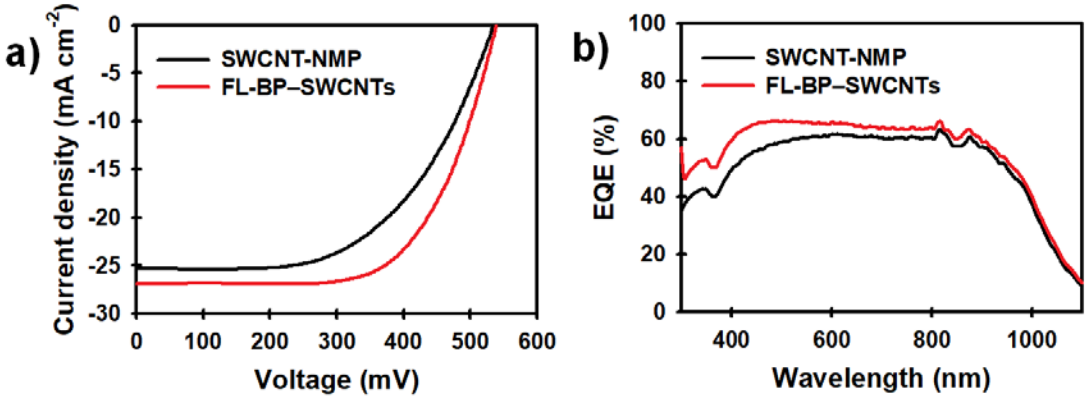

Figure 3-24. (a) J-V curves and (b) IPCE spectra of the best-performing solar cells fabricated with SWCNT films with and without FL-BP flakes.

Table 3-3. Detail PV characteristics of the best-performing solar cells prepared using SWCNT-NMP and FL-BP–SWCNT films obtained under both light and dark measurements.

Device	J_{sc}; (mA cm^{-2})	V_{oc}; (V)	FF	PCE; (%)	ideality	J_{sat}; (mA cm^{-2})
SWCNT-Si	**25.31**; 25.06 ± 0.36	**0.552**; 0.543 ± 0.013	**0.56**; 0.52 ± 0.02	**7.52**; 7.35 ± 0.25	1.42 ± 0.18	1.17 (± 1.36) x 10^{-5}
FL-BP–SWCNT-Si	**26.90**; 26.70 ± 0.28	**0.538**; 0.538 ± 0.001	**0.65**; 0.64 ± 0.01	**9.37**; 9.20 ± 0.25	1.22 ± 0.06	1.38 (± 0.77) x 10^{-6}

Furthermore, the most significant improvement recorded for the device after using FL-BP was in the FF value (increased from 0.56 to 0.65). The FF improvement for the PV devices containing FL-BP is mainly elucidated by the suppressed charge recombination rate.[19, 20] To investigate the infuence of FL-BP on the charge recombination rate of the cells, dark J-V curves were scanned, and the J_{sat} and ideality factor were obtained from the measurements (Table 3-3). The average ideality factor for the FL-BP–SWCNT films based devices was 1.22 ± 0.06, while the cell fabricated with SWNCT-NMP film was 1.42 ± 0.18. Importantly, the average J_{sat} of the solar cells with FL-BP–SWCNT-Si (1.38 (± 0.77) x 10^{-6} mA cm^{-2}) was significantly lower than that (1.17 (± 1.36) x 10^{-5} mA cm^{-2}) of only SWCNT

films based devices. The ideality factor close to 1 and lower J_{sat} of the PV cells indicate a lower charge recombination rate.[20] This reduced charge recombination rate can be due to the combination of improved film network and increased hole selectivity with the presence of FL-BP.

The PV characteristics of the devices were measured over 12 days with the cells left in ambient conditions to test their stability. It is well known that SWCNT-Si solar cells are not stable without encapsulation due to the oxidation of Si substrate.[21] In order to test the influence of FL-BP on the stability of the devices, no passivation on the devices was performed. As a result, there was no significant change in the device stability between the cells fabricated with and without FL-BP (Figure 3-25). This is not surprising as the porosity of the SWCNT films is very similar and hence the rate of oxidation of the Si would be unchanged. It does however again indicate the stability of the FL-BP which has been shown to degrade very quickly in other work over a week.[15] The fact that the decay rates for the two types of cells is the same shows that the added nanomaterial is not undergoing any significant degradation.

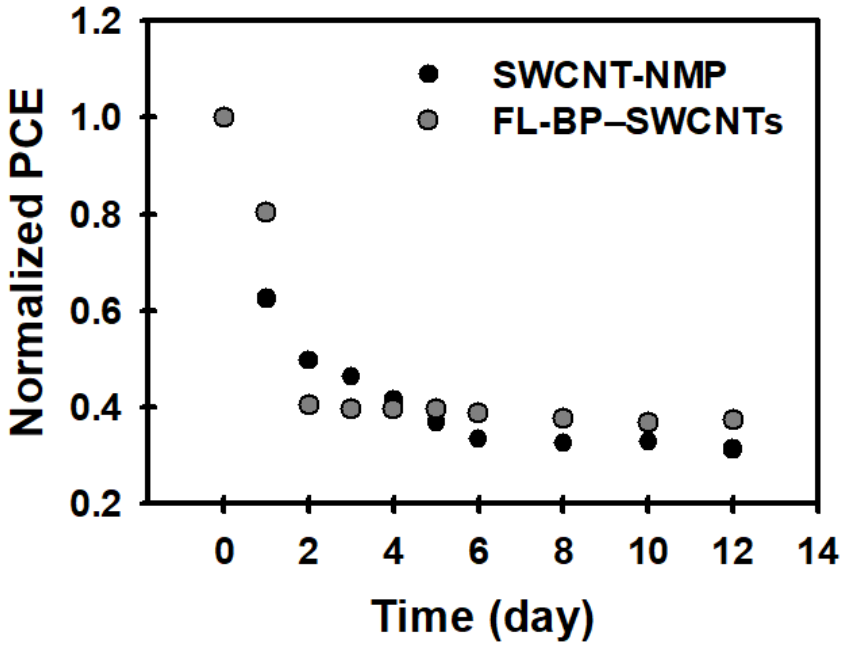

Figure 3-25. Stability test of the solar cells fabricated with and without FL-BP.

3.4. References

[1] M. Matsumoto, Y. Saito, C. Park, T. Fukushima, T. Aida, *Nat Chem*, **2015**, *7*, 730.

[2] C. Zhu, F. Xu, L. Zhang, M. Li, J. Chen, S. Xu, G. Huang, W. Chen, L. Sun, *Chem. Eur. J*, **2016**, *22*, 7357.

[3] Z. Liu, Y. Wang, Z. Wang, Y. Yao, J. Dai, S. Das, L. Hu, *Chem. Commun*, **2016**, *52*, 5757.

[4] P. Yasaei, B. Kumar, T. Foroozan, C. Wang, M. Asadi, D. Tuschel, J. E. Indacochea, R. F. Klie, A. Salehi-Khojin, *Adv. Mater*, **2015**, *27*, 1887.

[5] J. Pei, X. Gai, J. Yang, X. Wang, Z. Yu, D.-Y. Choi, B. Luther-Davies, Y. Lu, *Nat Commun*, **2016**, *7*, 10450.

[6] S. Zhang, J. Yang, R. Xu, F. Wang, W. Li, M. Ghufran, Y.-W. Zhang, Z. Yu, G. Zhang, Q. Qin, Y. Lu, *ACS Nano*, **2014**, *8*, 9590.

[7] B. Sa, Y.-L. Li, J. Qi, R. Ahuja, Z. Sun, *J. Phys. Chem. C*, **2014**, *118*, 26560.

[8] X. Zhang, H. Xie, Z. Liu, C. Tan, Z. Luo, H. Li, J. Lin, L. Sun, W. Chen, Z. Xu, L. Xie, W. Huang, H. Zhang, *Angew. Chem. Int. Ed*, **2015**, *54*, 3653.

[9] Z. Guo, H. Zhang, S. Lu, Z. Wang, S. Tang, J. Shao, Z. Sun, H. Xie, H. Wang, X.-F. Yu, P. K. Chu, *Adv. Funct. Mater*, **2015**, *25*, 6996.

[10] T. Ahmed, S. Balendhran, M. N. Karim, E. L. H. Mayes, M. R. Field, R. Ramanathan, M. Singh, V. Bansal, S. Sriram, M. Bhaskaran, S. Walia, *npj 2D Mater. Appl*, **2017**, *1*, 18.

[11] H. Liu, A. T. Neal, Z. Zhu, Z. Luo, X. Xu, D. Tománek, P. D. Ye, *ACS Nano*, **2014**, 8, 4033.

[12] W. Lu, H. Nan, J. Hong, Y. Chen, C. Zhu, Z. Liang, X. Ma, Z. Ni, C. Jin, Z. Zhang, *Nano Res*, **2014**, *7*, 853.

[13] A. Favron, E. Gaufres, F. Fossard, A.-L. Phaneuf-Lheureux, N. Y. W. Tang, P. L. Levesque, A. Loiseau, R. Leonelli, S. Francoeur, R. Martel, *Nat Mater*, **2015**, *14*, 826.

[14] M. Batmunkh, M. Bat-Erdene, J. Shapter, *Adv. Mater*, **2016**, *28*, 8586.

[15] J. Kang, J. D. Wood, S. A. Wells, J.-H. Lee, X. Liu, K.-S. Chen, M. C. Hersam, *ACS Nano*, **2015**, *9*, 3596.

[16] W. Zhao, Z. Xue, J. Wang, J. Jiang, X. Zhao, T. Mu, *ACS Appl. Mater. Interfaces*, **2015**, 7, 27608.

[17] L. Yu, D. Tune, C. Shearer, J. Shapter, *ChemSusChem*, **2015**, *8*, 2940.

[18] W. Chen, K. Li, Y. Wang, X. Feng, Z. Liao, Q. Su, X. Lin, Z. He, *J. Phys. Chem. Lett*, **2017**, *8*, 591.

[19] L. Yu, M. Batmunkh, T. Grace, M. Dadkhah, C. Shearer, J. Shapter, *J. Mater. Chem. A*, **2017**, 5, 8624.

[20] M. Batmunkh, T. J. Macdonald, C. J. Shearer, M. Bat-Erdene, Y. Wang, M. J. Biggs, I. P. Parkin, T. Nann, J. G. Shapter, *Adv. Sci*, **2017**, *4*, 1600504.

[21] D. D. Tune, B. S. Flavel, R. Krupke, J. G. Shapter, *Adv. Energy Mater*, **2012**, *2*, 1043.

Chapter 4.

Conclusion

4.1. Conclusions

In this thesis, we have demonstrated the production of high-quality few-layer black phosphorus (FL-BP) sheets using a facile, efficient and novel production based on microwave (MW)-assisted liquid-phase exfoliation (LPE) method. More importantly, our method requires extremely short processing time and does not involve use of any surfactant or ultrasonication. A diverse range of experimental investigations, combined with DFT calculation, have been carried out to assess the as-prepared FL-BP flakes. Our experimental coupled with theoretical studies have confirmed that the product synthesized using this MW technique is ultrathin FL-BP nanosheets. The solution of our FL-BP is well protected against degradation in ambient air and even water. Our FL-BP sheets prepared using this MW-assisted LPE have very large lateral dimensions, ranging from hundreds of nanometers up to ~4 μm. There is no doubt that the work presented in this thesis will open up a new research avenue for the preparation of phosphorene based thin films and hybrid materials for a wide range of applications.

As a proof of concept, our FL-BP sheets were successfully used to enhance the efficiency of SWCNT-Si solar cells. Interestingly, the NMP based FL-BP solution was found to be stable when mixed with water based SWCNT suspension. Due to their unique structure and *p*-type dominated conduction properties, the FL-BP sheets employed SWCNT-Si devices showed an improved charge transfer properties and suppressed charge recombination rate. As a result, impressive power conversion efficiency (PCE) of 9.37% was achieved using FL-BP incorporated cell, while the device without FL-BP showed a maximum efficiency of 7.52%. Therefore, this work also suggests that the solution processed phosphorene sheets are ideal candidates for high-performance PV devices.

The application of our high quality FL-BP solution is not just limited to only SWCNT-Si, they can also be successfully employed in many different types of application including batteries, supercapacitors, transistors and other types of solar cells such as dye-sensitized solar cells, organic solar cells and perovskite solar cells.

4.2. Future Directions and Recommendations

Although excellent achievements have been made in the prodution of FL-BP, a preparation approach that is low-cost, simple and can efficiently control the layer number of phosphorene is still required. In this regard, several alternative approaches that might be of great interest can be recommended: (i) Ball milling bulk BP before its exfoliation would be helpful as the van der Waals interaction between the layers can be weakened by this process. (ii) :lithiation is a promising method to prepare FL-BP sheets by inserting Li atoms into the BP layers as this method has successfully been used in many other 2D layered materials. (iii) Methods such as chemical vapor deposition (CVD), hydrothermal, solvothermal and self-assembly have been proven to be powerful bottom-up approaches to prepare a wide range of 2D materials. However, none of these approaches have been employed to prepare 2D phosphorene. Therefore successful preparation of 2D phosphorene using these approaches is expected to draw unprecedented attention.

Layer dependent bandgap, ambipolar semiconducting properties, high charge mobility and good flexibility are the major attractions of 2D phosphorene nanosheets. Benefiting from these outstanding properties, phosphorene and phosphorene based materials are likely to play critical roles in many emerging photovoltaic devices such as dye-sensitized solar cells, organic solar cells, quantum dot-sensitized solar cells and perovskite solar cells. In addition to phosphorene nanosheets, black phosphorus quantum dots are exciting new materials and have attracted increasing attention over the past very few years. It should be noted that the longer processing time method such as over 20 min of BP using our microwave-assisted LPE showed to produce ultrasmall quantums dots (see Figure 3-5d). There is still considerable scope for the use of these rising-star materials for emerging solar cells. Therefore we believe that black phosphorus derivatives including phosphorene nanosheets and black phosphorus quantum dots will have significant contribution to the future development of solar cell systems. Some important suggestions for the potential application of black phosphorus derivatives in particular type of solar cells can be listed as follows:

(i) 2D Phosphorene based heterostructures with other 2D layered materials like graphene are expected to be excellent candidates as hole transporting materials for organic solar cells due to the combination of p-type dominated semiconducting properties of phosphorene and high conductivity of graphene. Moreover, the composite material of phosphorene and *p*-NiO_x can be very promising hole transporting material for organic photovoltaic.

In addition to hole transporting layers, exploring the effect of BP derivatives in the TiO_2 nanostructures as electron transporting layer of organic solar cells would be an interesting strategy to enhance the device efficiency.

(ii) Recent theoretical studies suggested that phosphorene might be an ideal candidate for use in p-n heterojunction solar cells and predicted that these types of HJSCs can even achieve a PCE of as high as 20%, which makes them extremely competitive with other types of 2D heterojunctions. Phosphorene based van der Waals trilayer heterojunction structures such as phosphorene/TMDs/phosphorene based solar cells are also expected to show remarkably high efficiency. Although these computational investigations suggest considerable opportunities, there is currently no experimental data to confirm these theoretical predictions on such PV cells. Given this, phosphorene based HJSCs are likely to draw a much attention from the PV community in the near future.

(iii) Both DSSCs and QDSSCs have attracted significant attention because of their simple fabrication and low production cost. These PV devices are mainly fabricated on transparent conducting ITO or FTO coated substrates. We anticipate that phosphorene could be used to modify the interface between the ITO/FTO and charge transporting layer to reduce the rate of charge recombination, similar to interface functionalization methods using $TiCl_4$ or graphene which have proven effective methods to enhance the efficiencies of such solar cells.

Due to its high charge mobility and suitable energy levels, employing few-layer black phosphorus as a photoanode material to replace the conventional oxide semiconductors in DSSCs and QDSSCs would be very interesting. Additionally, there is very little doubt that DSSC and QDSSCs fabricated

with phosphorene incorporated oxide semiconductors (e.g. TiO_2, SnO_2) based photoanodes could exhibit high PCEs. In such device architectures, the high charge mobility of phosphorene can accelerate the electron transfer process and suppress the charge recombination rate.

Counter electrodes based on hybrid materials such as phosphorene incorporated nanocarbons (CNTs and graphene) can be expected to show improved efficiency of DSSCs. However, research studies on electrocatalytic properties of phosphorene and phosphorene-based materials are lacking.

(iv) Research into PSCs is currently the most attractive topic in the PV community due to their potential of producing remarkably high PCEs at reasonably low-cost. Because of its outstanding properties, phosphorene is likely to play significant roles in PSCs. Due to the suitable energy level of perovskite-phosphorene-TiO_2; phosphorene incorporated TiO_2 photoanodes based PSCs are potentially expected to exhibit very high PCEs. Phosphorene can also act as a bridge between the TiO_2 and perovskite, and so that the electrons transfer in very small energy steps from the perovskite to TiO_2 without an energy barrier. Low-temperature processed fabrication of phosphorene-based PSCs should be developed as phosphorene sublimes at 400^oC. If successful, this will undoubtedly open a new possibility for designing flexible devices.

Due to its high charge mobility and suitable energy levels (especially *p*-type dominated conduction type), phosphorene may be a promising alternative to the conventional Spiro-OMeTAD for PSCs. The oxidation of phosphorene under ambient conditions can lead to the formation of new insulating oxides and suboxides (unwanted) and result in poor stability, while the oxidation is desired to increase the conductivity by oxygen-doping. Therefore, optimization of these phosphorene parameters is required and would provide a rich area of research.

Appendix A

Theory detail

Optical absorption of phosphorene

We perform our density-functional theory (DFT) calculations with the Perdew-Burke- Ernzerhof exchange-correlation functional,[1] using the SIESTA code.[2] We perform geometry relaxation to obtain the ground state electronic structure at the Γ point, where the simulation box is 40 Å x 40 Å x 20 Å. SIESTA represents the basis sets in terms of numerical atomic orbitals, and approximates the ionic potential in terms of Troullier-Martins[3] norm-conserving pseudopotentials. The auxiliary basis uses a real-space mesh with a kinetic energy cutoff of 300 Ry, and the basis functions are radially confined using an energy shift of 0.005 Ry. In the structural energy minimization, the internal coordinates are allowed to relax until all of the forces are less than 0.01 eV/ Å.

CNT(6,5) – phosphorene interaction

To obtain the atomic and electronic structure of the isolated CNT(6,5) and the phosphorene island, we perform spin-unrestricted DFT calculations with the SIESTA code,[2] using the generalized gradient approximation for the exchange-correlation functional as developed by Perdew, Burke and Ernzerhof (PBE).[1] To accurately account for the weak interaction between CNT(6,5) and phosphorene, we applied the DRSLL[4] van der Waals' self-consistent dispersion correction. SIESTA uses basis sets comprised of numerical atomic orbitals, and approximates the atomic potential in terms of Troullier-Martins[3] norm-conserving pseudopotentials. The auxiliary basis uses a real-space mesh with a kinetic energy cut-off of 500 Ry, and the basis functions are radially confined using an energy shift of 0.005 Ry. We allow full atomic relaxation until the forces on the atoms are less than 0.03 eV/A. All of our calculations are performed at the Γ point.

Results and discussion

Furthermore, we studied the UV-vis absorbance of phosphorene by performing density-functional theory (DFT) calculations within the generalized gradient approximation by Perdew, Burke and Ernzerhof (PBE).[1] The optical absorption, I(ω) is computed as the imaginary part of the dielectric function in the linear response approximation,[5] and the optical absorbance is proportional to ωI(ω).[6] These optical calculations are performed with an incident polarization along the zigzag direction (the average optical spectrum for the armchair and zigzag polarizations is qualitatively similar to the zigzag polarization; and therefore here we only adopt the zigzag polarization). The experimental results were compared to a periodic 2D monolayer structure and the two H-passivated phosphorene clusters, namely $P_{77}H_{25}$ (small island) and $P_{252}H_{46}$ (island), illustrated in Figure A-1a. The spectra of these structures, in comparison with the experimental spectrum of 11 min MW-exfoliated BP, are displayed in Figure A-1b. In general, the UV-vis spectra of the three phosphorene structures qualitatively agree with the experimental spectrum in terms of possessing three characteristic peaks within the range 200-400 nm (centered at 230 nm, 300 nm and 370 nm in the experimental spectrum). In the three theoretical spectra in Figure A-1b, we can clearly observe the trend in the positions of the spectral peaks as we go from the small island to the 2D phosphorene sheet: as the cluster becomes larger, the three characteristic peaks redshift towards their position in the 2D sheet.

However, an important distinction between the experimental spectrum and the 2D spectrum in the features of the three major peaks in the range 200-400 nm is that the rightmost peak at ~350 nm is higher in intensity than the other peaks. However, in the experimental spectrum, the middle peak (at ~300 nm) has the highest intensity, and this behavior is exhibited in the spectrum of the $P_{252}H_{46}$ cluster. Therefore, the synthesized phosphorene is simulated by large H-terminated phosphorene sheets with reasonable accuracy. Notably, these slight differences in the peak intensities and some peak shifts observed between the theoretical spectra and experimental spectrum are probably due to the fact that our FL-BP sample produced using MW-exfoliation method consists of few-layer to multi-layer and small- and large- area flakes, which are in excellent agreement with the other characterizations reported in this work.

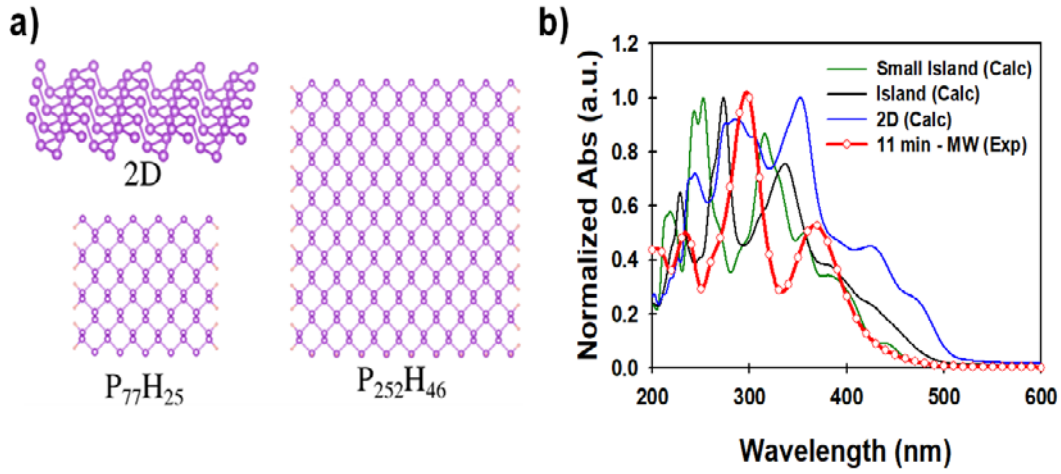

Figure A-1. (a) The atomic structure of the 2D monolayer structure and two H-passivated phosphorene clusters ($P_{77}H_{25}$ (small island) and $P_{252}H_{46}$ (island)). (b) Comparison of the absorption spectra of phosphorene in the UV-vis region obtained by DFT and experiment.

To obtain further insight into the nature of the interaction between the CNT and phosphorene, we perform DFT calculations, within the generalized gradient approximation (GGA),[1] to investigate the adsorption of a monolayer phosphorene, $P_{77}H_{25}$, and bilayer phosphorene, $2(P_{77}H_{25})$, flakes on a unit cell of CNT(6,5), and the influence of such adsorption on the electronic properties. The GGA results were compared with those obtained by applying the DRSLL[4] correlation correction to account for van der Waals forces. The adsorption of a larger phosphorene flake, $P_{110}H_{30}$ was also investigated to examine whether the size of the BP flake would have an influence on the results. The $P_{77}H_{25}$-CNT(6,5), $2(P_{77}H_{25})$-CNT(6,5), and the $P_{110}H_{30}$-CNT(6,5) structures are depicted in Figure A-2. The band gap obtained for the isolated CNT(6,5) using GGA is 1.07 eV, which is ~0.3 eV lower than the experimentally measured value, due to the tendency of DFT to underestimate the bandgap. The PBE calculated band gap of $P_{77}H_{25}$, and $P_{110}H_{30}$ are 1.74 eV and 1.46 eV, respectively. Since P3-SWNT was used in our experiment, CNT(6,5) was selected for the calculation as P3-SWNT contains a large amount of nanotube (6,5).

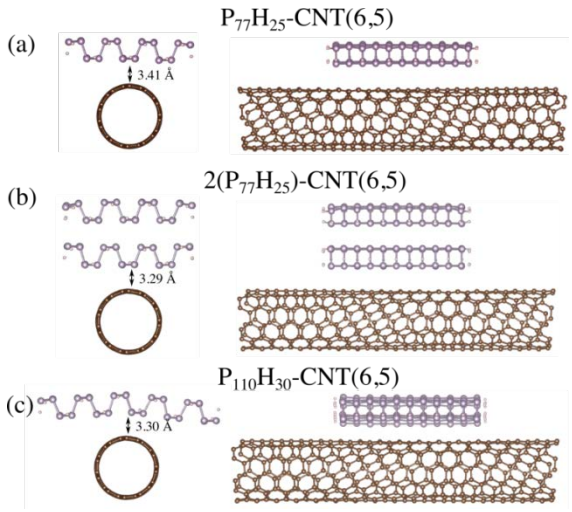

Figure A-2. Atomic structure of (a) $P_{77}H_{25}$-CNT(6,5), (b) 2($P_{77}H_{25}$)-CNT(6,5), and (c) $P_{110}H_{30}$-CNT(6,5) structures, showing the front view (left) and side view (right). The distance between the phosphorene flake and CNT are obtained using the DRSLL van der Waals correction, and are displayed.

To obtain further insight into the nature of the interaction between the CNT and phosphorene, DFT calculations were undertaken for the structures shown in Figure A-2. The PV efficiency observed in the phosphorene-CNT(6,5) structures can be understood in the light of the analysis of the partial density of states (PDOS), which displays the band alignment in a DSSC dye-surface interaction, where the lowest-unoccupied molecular orbital (LUMO) of the absorber is larger than the valence band minimum (VBM) of the surface,[7] thus indicating that electrons will experience a transition from the excited state into the surface. Here we treat the phosphorene fragment as the photosensitive component, while the substrate is CNT(6,5). This hybrid structure can also be viewed as a donor-acceptor complex, where the phosphorene is the donor, while CNT is the acceptor species.[8] A similar method has been used for studying donor-acceptor complexes made from H-terminated phosphorene and F-terminated phosphorene, where the former acted as a donor, while the later an acceptor.[9]

Figure A-3 illustrates the PDOS for both $P_{77}H_{25}$-CNT(6,5) and 2($P_{77}H_{25}$)-CNT(6,5), calculated within the GGA. In $P_{77}H_{25}$-CNT(6,5), the LUMO of phosphorene is 0.45 eV higher than the LUMO of CNT(6,5). In 2($P_{77}H_{25}$)-CNT(6,5), the LUMO of the bilayer phosphorene is 0.3 eV higher than the LUMO of CNT(6,5). The calculations

for $P_{110}H_{30}$-CNT(6,5) give a similar trend, where the BP LUMO is 0.41 eV higher than the LUMO in CNT. These trends are consistent with those obtained from the DRSLL correction. Therefore, the calculations establish that in the phosphorene-CNT(6,5) structure, the phosphorene acts as an electron donor which would readily donate electrons to the CNT(6,5) acceptor upon optical excitation. The behaviour is exhibited by a monolayer phosphorene flake with two different sizes, and also by a bilayer phosphorene flake, which can be generalized to the case of FL-BP flakes with a few layers of phosphorene, such as those synthesized in the present experiment. This transfer of electron density to the CNTs n-dopes the nanotubes and leaving behind phosphorene which can now accept holes. In the devices, this will improve the transfer of holes from the depletion region at the interface to the FL-BP–SWCNT films, leading to the improved J_{sc} observed.

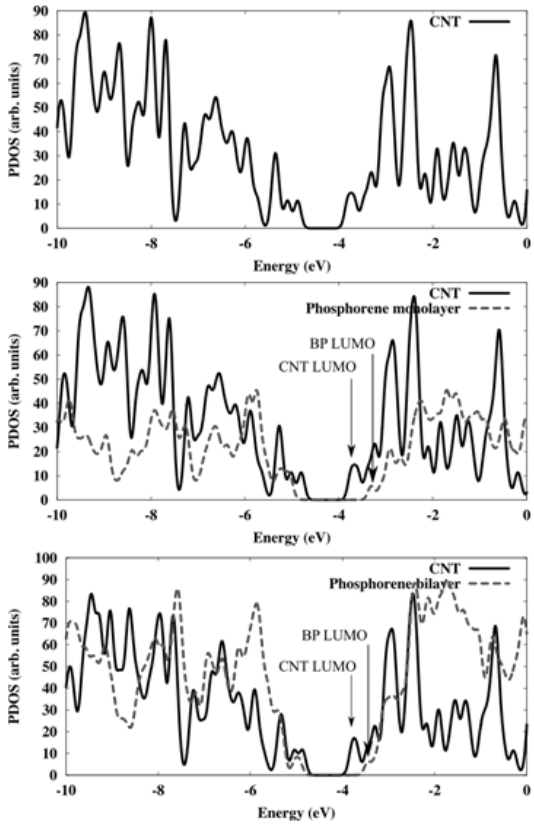

Figure A-3. The partial density of states (PDOS) for the CNT (6,5) (top), $P_{77}H_{25}$-CNT(6,5) (middle) and 2($P_{77}H_{25}$)-CNT(6,5) (bottom) systems. The vertical arrows indicate the position of the LUMO for the subsystems.

Note: $P_{77}H_{25}$ and $P_{252}H_{46}$ are not infinite and in fact the formula are provided to show that “islands” of phosphorene were considered. The islands are H terminated on the edges to ensure no free electrons but passivation in other directions is not required as binding is completed. Additionally there were calculations for infinite sheets. Importantly there are size effects for the positions of the peaks in question with varying sizes of phosphorene layers and these calculations are ongoing.

References

[1] J. P. Perdew, K. Burke, M. Ernzerhof, *Phys. Rev. Lett*, **1996**, *77*, 3865.

[2] M. S. José, A. Emilio, D. G. Julian, G. Alberto, J. Javier, O. Pablo, S.-P. Daniel, *J. Phys.: Condens. Matter*, **2002**, *14*, 2745.

[3] N. Troullier, J. Martins, *Solid State Commun*, **1990**, *74*, 613.

[4] M. Dion, H. Rydberg, E. Schröder, D. C. Langreth, B. I. Lundqvist, *Phys. Rev. Lett*, **2004**, *92*, 246401.

[5] P. Yu, M. Cardona, *Fundamentals of Semiconductors*, **2010**, *4*, DOI: 10.1007/978.

[6] L. Matthes, P. Gori, O. Pulci, F. Bechstedt, *Phys. Rev. B*, **2013**, *87*, 035438.

[7] W. Ma, Y. Jiao, S. Meng, *J. Phys. Chem. C*, **2014**, *118*, 16447.

[8] R. Zhang, B. Li, J. Yang, *J. Phys. Chem. C*, **2015**, *119*, 2871.

[9] W. Hu, L. Lin, C. Yang, J. Dai, J. Yang, *Nano Lett*, **2016**, *16*, 1675.